X-RAY VARIABILITY OF GX 339−4 IN ITS VERY HIGH STATE

SIGENORI MIYAMOTO, KAZUHIRO KIMURA,[1] AND SHUNJI KITAMOTO

Department of Physics, Faculty of Science, Osaka University, Machikaneyama 1-1, Toyonaka, Osaka, 560, Japan

AND

TADAYASU DOTANI AND KEN EBISAWA

Institute of Space and Astronautical Science, Yoshinodai 3-1-1, Sagamihara, Kanagawa, 229, Japan

ABSTRACT

GX 339−4 was observed with the large area counters (LAC) onboard *Ginga* in its very high state, where the X-ray intensity was about a factor of 2–3 larger than its high state and it showed very rapid variations on time scales of less than several minutes, which had not been observed earlier in the high state of this source. The X-ray energy spectrum was very soft; it consisted of a low-energy component and a high-energy tail. The low-energy component could be interpreted as being due to disk blackbody radiation (the disk blackbody component) and the high-energy tail as being due to Compton-scattering radiation (the Comptonized black-body component). The X-ray energy spectrum also showed K-edge absorption of highly ionized iron atoms of about 10^{19} cm^{-2} and an iron emission line with an equivalent width of about 60–100 eV.

On short time scales of less than several minutes, the X-rays showed rapid time variations. For instance, in power spectral density functions, 6 Hz quasi-periodic oscillations (QPOs), very low frequency noise (VLF noise), and low-frequency noise (LF noise) were recognized. There are three types of power spectral density functions. Time variations such as dips and flip-flops were also observed. These rapid time variations are due to the Comptonized blackbody component.

On long time scales larger than hours, the disk blackbody component and the Comptonized blackbody component changed independently. However, these changes took place within some restricted regions in an X-ray hardness ratio (color)–intensity or a color-color diagrams. These are a hardness ratio increasing (with the X-ray flux) branch, a hardness ratio decreasing branch, and their crossing region. These two energy spectral branches and their crossing region have three different types of power density spectra: these different branches and regions have different time variations on time scales of less than several minutes. In the hardness ratio increasing branch, the hard Compton-scattering component is the main cause of the long-term time variation of the X-ray flux, and in the hardness ratio decreasing branch, the disk blackbody component is the main cause of the long-term time variation of the X-ray flux.

On a time lag versus Fourier period diagram, the time lag between time variations of different energy X-rays showed shoulder structures in addition to the large time lags at large Fourier periods similar to those observed in Cygnus X-1. The time variations of the X-rays of 2.3–4.6 keV were most advanced: time variations of X-rays with both lower and higher energy than 2.3–4.6 keV showed time lags relative to those of 2.3–4.6 keV X-rays. These facts together with the X-ray energy spectrum can be explained in terms of a high-energy component being due to a Compton-scattering cloud of size of about 10^9 cm, temperature kT_e of about 30 keV, and Thomson scattering depth of about 0.5–1.0; the variable blackbody radiation with $kT = \sim 1$ keV is incident to the large Compton-scattering cloud.

Subject headings: stars: individual (GX 339−4) — X-rays: binaries — X-rays: spectra

1. INTRODUCTION

The X-ray source GX 339−4 (4U 1658−48) has been considered to be one of the black hole candidates, because it has a high state with an ultrasoft energy spectrum and a low state with a hard energy spectrum, and it shows random fast time variation of the X-ray intensity in its low state like Cygnus X-1 (Makishima et al. 1986; Ilovaisky et al. 1986). The X-ray behavior of GX 339−4 has been studied with various satellites including *OSO 7* (Markert et al. 1973), *HEAO 1* (Samimi et al. 1979; Nolan et al. 1982), *Hakucho* (Maejima et al. 1984), *Ariel 6* (Motch et al. 1983; Ricketts 1983), *Tenma* (Makishima et al. 1986), and *EXOSAT* (Ilovaisky et al. 1986).

[1] Now at Kasima Space Communication Center, Communication Research Laboratory, Hirai 893-1, Kasima-cho, Kasima-gun, Ibaragi, 314, Japan.

GX 339−4 in its high state was observed by Makishima et al. (1986). The X-ray spectrum of GX 339−4 in its high state (0.6–0.8 counts s^{-1} in 2–10 keV; 300–400 μJy) comprised a very low energy component, which could be explained by a disk-blackbody model (Mitsuda et al. 1984) and a high-energy tail having a power-law shape of the photon number index of about −0.9 to −2.1. The intensity of the high-energy tail gradually changed on a time scale of days; however, the very soft component was stable on this time scale. Short-term variations of X-rays were small; periodic or aperiodic variations in excess of the Poisson noise could not be found in the 2–10 keV X-ray data on a time scale of 15.6 ms to 20 minutes. GX 339−4 in its high state was also observed by Ilovaisky et al. (1986). The energy spectrum was fitted with a combination of a very soft component having a soft unsaturated Comptonized spectrum and a power-law component with a photon number index of

−2.2 ± 0.2. They set an upper limit of 0.8% to any X-ray variability from 1 s to 6 hr.

In the low state, the energy spectrum is harder than in the high state. The energy spectrum can be expressed by a power law with a photon number index of about −1.5 (Ricketts 1983). Its X-ray intensity shows rapid time variations. For instance, Samimi et al. (1979) observed that the intensity changed up to a factor of 3 with the rise time as short as 40 ms when its X-ray intensity was about 50 μJy. Maejima et al. (1986) found that the time variations in the low state (the X-ray intensity of about 100–200 μJy) continued for at least 1 week and that the root mean square amplitude of the variation was 30%–40% of its intensity on time scales of a fraction of a second to tens of seconds.

In the off state, the X-ray intensity becomes about 1–2 μJy. Ilovaisky et al. (1986) found that in this state (about 1.5 μJy) GX 339−4 had an energy spectrum of a power law of the photon number index of about −1.7. Aperiodic variations in the X-ray intensity were less than 26% on time scales from 20 s to 6 hr. Nolan et al. (1982) observed high-energy X-rays of 20–200 keV even in its off state and fitted their energy spectrum by a combination of a thin thermal bremsstrahlung component and a power-law component.

The optical counterpart of GX 339−4 is a faint blue star with a photographic magnitude of 16.0–18.5 (Doxsey et al. 1979; Grindlay 1979). It becomes sometimes exceptionally faint at $B > 21$ (Hutchings, Cowley, & Crampton 1981; Ilovaisky & Chevalier 1981). It has strong Balmer emission and He II emission lines (Grindlay 1979). The optical flux showed erratic variations of about 1 mag on a time scale of hours (Grindlay 1979) and also quasi oscillations with a mean period of 20 s (30%–40% full amplitude) together with very short time scale activity such as a flare as short as 10–20 ms, during which the flux increased by a factor up to 5 (Motch, Ilovaisky, & Chevalier 1982). The occurrence of optical states corresponding to the X-ray states was found by Motch et al. (1983) and Motch, Ilovaisky, & Chevalier (1985).

The distance to GX 339−4 was estimated to be about 4 kpc based on the assumption that the X-ray luminosity was similar to Cyg X-1 (Doxsey et al. 1979). Makishima et al. (1986) estimated it to be 3.5 kpc on the assumption of the standard candle of $M_v = 1.2$ for the low-mass binary X-ray stars (van Paradijs 1980). Grindlay et al. (1979) estimated the distance to be about 8 kpc, but they could not exclude a distance of 2–3 kpc. Cowley, Crampton, & Hutchings (1987) estimated the distance to be about 4 kpc from optical observations of the interstellar lines and the color. Hereafter, we will assume the distance to be 4 kpc.

We observed GX 339−4 with the large area proportional counters (LAC) onboard Ginga. The effective area of the LAC is 4000 cm². The flux was about 2 counts s⁻¹ cm⁻² in the energy range of 1.2–37.0 keV, which was about a factor of 2–3 larger than the intensities previously observed by Makishima et al. (1986) (0.6–0.8 counts s⁻¹ cm⁻²). Though Makishima et al. did not find any fast time variations, we found that the X-ray intensity showed rapid variations on time scales of less than several minutes, including 6 Hz QPO and short decreases of time duration of about 10–60 s (dips and flip-flops). This is the first observation of rapid X-ray intensity variations in the high state, and we will call this the very high state because GX 339−4 showed a quite different X-ray behavior in its high state.

2. OBSERVATIONS AND RESULTS

2.1. The X-Ray Light Curve

GX 339−4 has been observed with the all-sky monitor (ASM) onboard Ginga since the beginning of its observation (1987 March 6). The X-ray flux observed with ASM is shown in Figure 1. On 1988 August 9, this source increased up to about 0.5 counts s⁻¹ cm⁻² (1–6 keV) (∼290 μJy) and continued to rise. The observation of the source with LAC was performed from 1988 September 3 to September 7 in its very high state, and the observation time with LAC is shown by an arrow in Figure 1. The peak flux was about 2 counts s⁻¹ cm⁻² in the energy of 1.2–37 keV. The LAC observation was performed with the telemeter modes of MPC-1, MPC-2, MPC-3, and PC with a high and a medium bit rate. Details of the LAC and the telemeter modes were described by Turner et al. (1989).

The X-ray light curves of GX 339−4, observed with LAC with the MPC mode, are shown in Figure 2 in four energy ranges together with the hardness ratios. The data shown are background-subtracted and aspect-corrected.

2.2. The Energy Spectrum

The energy spectrum of GX 339−4 was very soft, and it had a high-energy tail. No single model of conventional form, including power-law, thin thermal, blackbody, and disk blackbody (Mitsuda et al. 1984; Makishima et al. 1986), could describe the observed spectrum of GX 339−4. Therefore we tried several two-component models to describe the spectrum, which were the blackbody, the disk blackbody, the power-law, and the exponential function for the very soft component and the power-law for the high-energy tail. These were not acceptable because of the large reduced χ^2 values. The best-fit models were those of the disk blackbody for the very soft component and the power-law for the high-energy tail, and their best-fit parameters are shown in Table 1A for a comparison to previous results, and an example is shown in Figure 3a.

Finally we found that the spectrum could be represented by a two-component model: a disk blackbody and a Comptonized blackbody component, together with large absorption
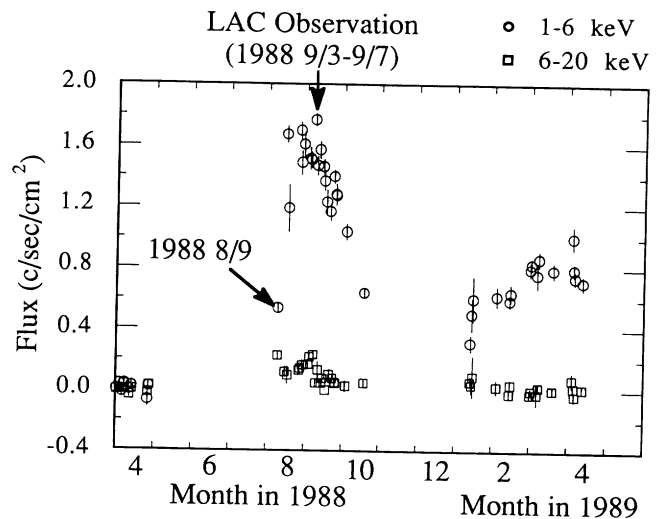

FIG. 1.—The X-ray intensities and the hardness ratios observed with Ginga ASM. The observation time by Ginga LAC is indicated by an arrow.
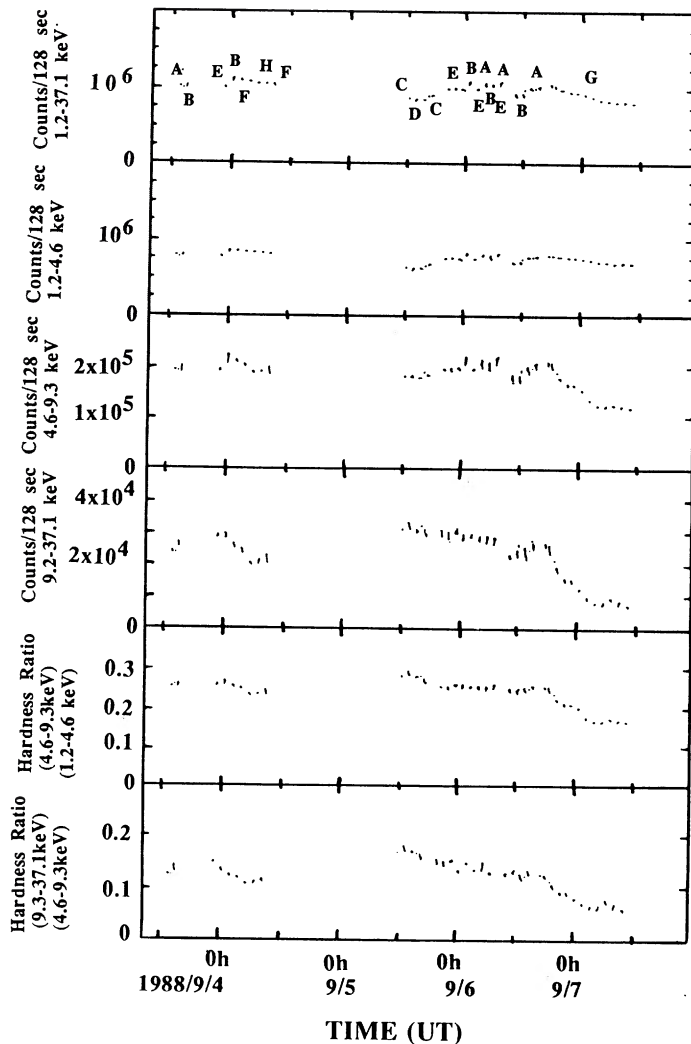
FIG. 2.—The X-ray intensities and the hardness ratios observed with *Ginga* LAC with the MPC mode. The power spectral states are also shown.

of the iron (Fe^{+24}) K-edge of 8.8 keV, the interstellar absorption and an iron emission line. The results are shown in Table 2. (In the above model, if we choose a power-law component instead of the Comptonized blackbody component, the reduced χ^2 values of the fitting have larger values than about 2 in about one half of the observed spectra as shown in Table 1B.) The disk blackbody component is based on the standard accretion disk model (Shakura & Sunyaev 1973) and on the assumption that the accretion disk is optically thick and radiates as a blackbody with a temperature that changes throughout the disk (Pringle 1981; Mitsuda et al. 1984; Hoshi 1984; Makishima et al. 1986; Mitsuda et al. 1989). The Comptonized blackbody component is the radiation scattered by a hot cloud; the initial photons are due to low-temperature blackbody radiation injected into the homogeneous isothermal hot cloud (Nishimura, Mitsuda, & Itho 1986)[2]. The K-edge absorption of helium-like iron ions (Fe^{+24}) was necessary to obtain good fits. We also added an iron emission line of zero line width.

[2] This calculation is for Comptonization in an infinite, isothermal, plane-parallel plasma cloud.
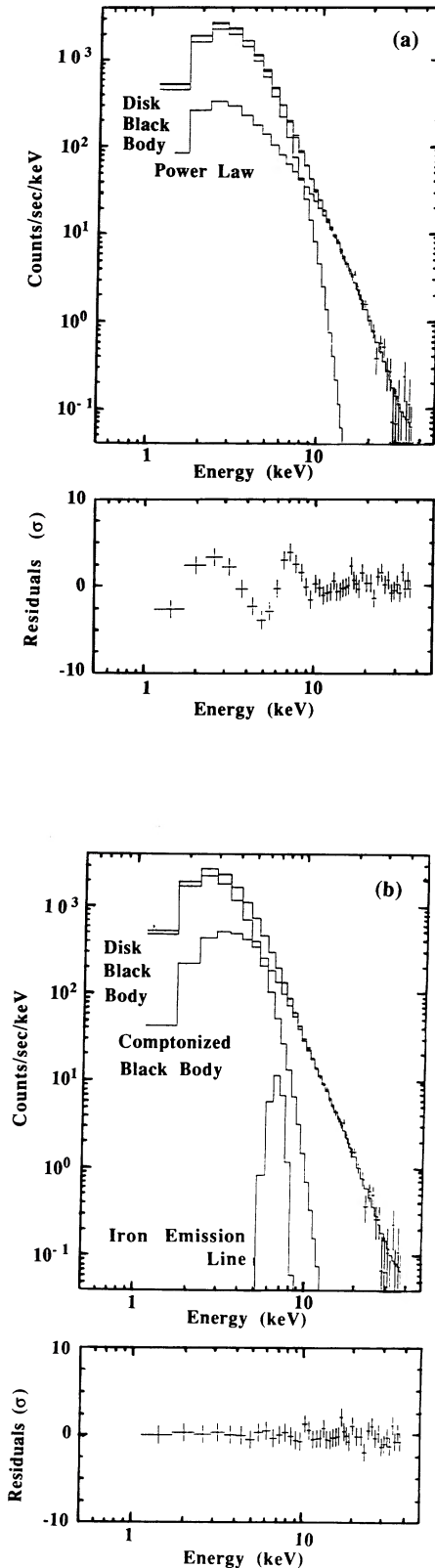

FIG. 3.—The energy spectrum of GX 339−4 in the power spectral state G at 00:33–00:35, 1988 September 7. (a) The fitting with a model of a disk blackbody component and a power-law component. (b) The fitting with a model of a disk blackbody component, a Comptonized blackbody component, the 8.8 keV K-edge absorption, and an iron line.

TABLE 1A

Best-Fit Parameters of the Model of Disk Blackbody and of Power Law

Time		Disk Black Body Rin $(\cos(i))^{0.5}$ (D/4kpc)km	kTin (keV)	Power Law Scale $(D/4kpc)^2 \times 10^{39}$	Index	Log(N_H) cm^{-2}	red. χ^2 d.o.f=41
9/4	01:56-02:16	$13.9^{\pm}1.9$	$0.951^{\pm}0.003$	$9.29^{\pm}0.10$	$2.480^{\pm}0.004$	$21.586^{\pm}0.026$	5.583
	03:34-03:54	$13.4^{\pm}3.0$	$1.005^{\pm}0.009$	$8.32^{\pm}0.62$	$2.501^{\pm}0.028$	$21.549^{\pm}0.057$	4.008
	05:13-05:33	$13.6^{\pm}3.0$	$0.999^{\pm}0.009$	$7.84^{\pm}0.59$	$2.508^{\pm}0.029$	$21.539^{\pm}0.062$	4.416
	06:49-07:10	$14.6^{\pm}3.2$	$0.976^{\pm}0.008$	$7.08^{\pm}0.55$	$2.525^{\pm}0.029$	$21.552^{\pm}0.057$	4.411
	08:25-08:38	$14.0^{\pm}3.1$	$0.986^{\pm}0.009$	$8.29^{\pm}0.71$	$2.550^{\pm}0.033$	$21.581^{\pm}0.057$	3.671
	08:38-08:49	$14.3^{\pm}3.2$	$0.981^{\pm}0.009$	$6.75^{\pm}0.64$	$2.504^{\pm}0.036$	$21.522^{\pm}0.064$	3.668
9/5	19:58-20:18	$12.7^{\pm}3.0$	$0.984^{\pm}0.011$	$7.88^{\pm}0.34$	$2.419^{\pm}0.026$	$21.364^{\pm}0.092$	4.961
	21:20-21:40	$12.8^{\pm}3.1$	$0.986^{\pm}0.010$	$7.26^{\pm}0.49$	$2.395^{\pm}0.025$	$21.348^{\pm}0.090$	5.559
	21:39-21:43	$13.9^{\pm}3.6$	$0.949^{\pm}0.013$	$9.75^{\pm}0.10$	$2.525^{\pm}0.041$	$21.577^{\pm}0.071$	4.282
	22:46-23:30	$12.5^{\pm}3.0$	$0.987^{\pm}0.011$	$7.97^{\pm}0.52$	$2.413^{\pm}0.025$	$21.405^{\pm}0.081$	5.877
9/6	00:24-00:46	$12.9^{\pm}2.9$	$1.011^{\pm}0.010$	$7.27^{\pm}0.51$	$2.411^{\pm}0.026$	$21.437^{\pm}0.074$	4.429
	02:02-02:12	$13.1^{\pm}3.2$	$0.978^{\pm}0.011$	$7.44^{\pm}0.57$	$2.402^{\pm}0.029$	$21.432^{\pm}0.080$	4.791
	02:12-02:13	$14.1^{\pm}4.2$	$0.938^{\pm}0.017$	$10.43^{\pm}1.69$	$2.539^{\pm}0.069$	$21.601^{\pm}0.097$	2.143
	02:14-02:17	$13.3^{\pm}3.6$	$0.957^{\pm}0.014$	$11.08^{\pm}1.17$	$2.548^{\pm}0.042$	$21.604^{\pm}0.070$	3.342
	02:18-02:24	$13.1^{\pm}3.4$	$0.966^{\pm}0.012$	$9.40^{\pm}0.85$	$2.499^{\pm}0.035$	$21.532^{\pm}0.072$	5.127
	03:40-04:03	$13.1^{\pm}3.0$	$0.988^{\pm}0.010$	$7.56^{\pm}0.51$	$2.425^{\pm}0.025$	$21.477^{\pm}0.068$	4.512
	05:18-05:41	$13.1^{\pm}3.1$	$0.990^{\pm}0.010$	$7.26^{\pm}0.47$	$2.406^{\pm}0.024$	$21.453^{\pm}0.071$	4.177
	06:54-07:18	$12.7^{\pm}2.9$	$1.013^{\pm}0.010$	$8.70^{\pm}0.59$	$2.485^{\pm}0.025$	$21.545^{\pm}0.058$	3.970
	10:08-10:24	$11.8^{\pm}2.9$	$0.991^{\pm}0.012$	$9.80^{\pm}1.08$	$2.612^{\pm}0.043$	$21.639^{\pm}0.060$	3.530
	17:42-17:47	$13.3^{\pm}3.2$	$0.991^{\pm}0.012$	$9.85^{\pm}1.11$	$2.560^{\pm}0.043$	$21.638^{\pm}0.059$	3.165
	18:23-18:44	$13.0^{\pm}2.9$	$1.001^{\pm}0.010$	$8.63^{\pm}0.77$	$2.537^{\pm}0.035$	$21.550^{\pm}0.063$	3.386
	19:38-19:41	$14.1^{\pm}3.4$	$0.972^{\pm}0.011$	$8.19^{\pm}1.12$	$2.567^{\pm}0.055$	$21.609^{\pm}0.068$	3.028
	20:00-20:23	$14.5^{\pm}3.1$	$0.971^{\pm}0.008$	$5.66^{\pm}0.49$	$2.492^{\pm}0.033$	$21.480^{\pm}0.067$	3.773
	21:36-21:59	$14.8^{\pm}3.1$	$0.964^{\pm}0.007$	$4.56^{\pm}0.42$	$2.487^{\pm}0.035$	$21.438^{\pm}0.071$	4.610
	22:53-23:13	$15.2^{\pm}3.2$	$0.954^{\pm}0.007$	$5.37^{\pm}0.51$	$2.558^{\pm}0.036$	$21.538^{\pm}0.059$	3.912
9/7	00:33-00:35	$16.2^{\pm}3.8$	$0.929^{\pm}0.010$	$5.83^{\pm}1.30$	$2.677^{\pm}0.090$	$21.589^{\pm}0.078$	2.680
	00:35-00:50	$15.3^{\pm}3.1$	$0.956^{\pm}0.007$	$3.21^{\pm}0.36$	$2.431^{\pm}0.043$	$21.417^{\pm}0.076$	3.642
	02:07-02:28	$18.0^{\pm}3.6$	$0.902^{\pm}0.006$	$1.74^{\pm}0.19$	$2.290^{\pm}0.041$	$21.547^{\pm}0.056$	2.744
	03:45-03:46	$19.2^{\pm}5.1$	$0.865^{\pm}0.012$	$3.96^{\pm}1.63$	$2.693^{\pm}0.178$	$21.713^{\pm}0.077$	1.405
	03:50-04:08	$18.2^{\pm}3.8$	$0.890^{\pm}0.006$	$1.56^{\pm}0.22$	$2.323^{\pm}0.056$	$21.576^{\pm}0.050$	2.227
	05:21-05:45	$17.8^{\pm}3.8$	$0.895^{\pm}0.006$	$1.25^{\pm}0.20$	$2.245^{\pm}0.060$	$21.538^{\pm}0.059$	2.486
	06:57-07:23	$17.1^{\pm}3.5$	$0.902^{\pm}0.006$	$1.64^{\pm}0.18$	$2.278^{\pm}0.043$	$21.500^{\pm}0.058$	2.696
	08:35-09:02	$17.5^{\pm}3.6$	$0.897^{\pm}0.006$	$1.45^{\pm}0.19$	$2.277^{\pm}0.050$	$21.542^{\pm}0.053$	2.791
	10:15-10:27	$17.8^{\pm}3.9$	$0.888^{\pm}0.007$	$1.85^{\pm}0.44$	$2.425^{\pm}0.094$	$21.607^{\pm}0.054$	2.447

The fitting results are shown in Table 2, where kT_{in} and r_{in} are the parameters of the disk blackbody component and the temperature and the radius of the innermost part of the accretion disk, respectively. The parameters kT_{bb} and S_{bb} are the temperature and the surface area of the blackbody radiation which are assumed to be incident to a Compton cloud; kT_e and τ are the temperature and the Thomson scattering depth of the Compton cloud. The iron emission line is expressed by an equivalent width and its energy E_{Fe}, and the K-edge absorption by Fe^{+24} atoms is represented by the column density

$N(Fe^{+24})$. The K-edge energy was fixed to be 8.8 keV. The interstellar absorption is expressed by N_H using Morrison & McCammon's calculation (1983). An example of the fits is shown in Figure 3b. The X-ray source was in the power spectral state G (see § 2.3).

From Table 2, we find that the innermost radius (R_{in}) and the temperature (kT_{in}) of the X-ray–emitting disk are about 25–30 km and 0.7–0.8 keV, respectively. The incident photons to the Compton cloud have a blackbody spectrum with a temperature (kT_{bb}) of about 1 keV; the temperature is a little

TABLE 1B

BEST-FIT PARAMETERS OF THE MODEL CONSISTING OF A DISK BLACKBODY AND A POWER LAW INCLUDING AN IRON K-LINE AND AN IRON K-EDGE ABSORPTION

| Time | | Disk Black Body | | Power Law | | Equ.W. | E_{Fe} | Log N_{Fe} | Log(N_H) | red. χ^2 |
		R_{in} $(\cos(i))^{0.5}$ (D/4kpc)km	kT_{in} (keV)	Scale $(D/4kpc)^2 \times 10^{39}$	Index	(eV)	(keV)	(cm^{-2})	(cm^{-2})	(dof=38)
9/4	01:56-02:16	15.2 ± 0.6	0.941 ± 0.018	13.4 ± 1.7	2.658 ± 0.047	96.1 ± 26.2	6.67 ± 0.14	18.73 ± 0.15	21.78 ± 0.06	1.97
	03:34-03:54	15.4 ± 0.6	0.934 ± 0.016	13.3 ± 1.9	2.683 ± 0.050	90.0 ± 25.6	6.63 ± 0.15	18.76 ± 0.13	21.79 ± 0.06	2.49
	05:13-05:33	16.4 ± 0.7	0.924 ± 0.015	10.5 ± 1.7	2.663 ± 0.055	95.4 ± 28.0	6.72 ± 0.15	18.74 ± 0.15	21.75 ± 0.06	2.11
	06:49-07:10	16.8 ± 0.7	0.905 ± 0.016	13.7 ± 2.0	2.745 ± 0.050	103.8 ± 29.9	6.51 ± 0.15	18.90 ± 0.10	21.82 ± 0.05	1.86
	08:25-08:38	15.9 ± 0.7	0.921 ± 0.018	14.2 ± 2.2	2.730 ± 0.054	86.8 ± 27.6	6.58 ± 0.17	18.79 ± 0.13	21.82 ± 0.06	2.02
	08:38-08:49	16.5 ± 0.7	0.910 ± 0.017	12.7 ± 2.1	2.714 ± 0.058	103.0 ± 29.1	6.55 ± 0.15	18.85 ± 0.12	21.80 ± 0.06	1.65
9/5	19:58-20:18	15.9 ± 0.8	0.880 ± 0.020	13.2 ± 1.4	2.591 ± 0.038	107.4 ± 26.3	6.58 ± 0.13	18.84 ± 0.10	21.76 ± 0.06	2.09
	21:20-21:40	16.2 ± 0.9	0.878 ± 0.021	13.0 ± 1.4	2.587 ± 0.038	105.3 ± 26.6	6.48 ± 0.14	18.90 ± 0.09	21.77 ± 0.06	2.51
	21:39-21:43	17.9 ± 1.2	0.840 ± 0.024	16.1 ± 2.2	2.680 ± 0.050	105.2 ± 32.7	6.40 ± 0.17	18.97 ± 0.09	21.87 ± 0.06	1.71
	22:46-23:30	16.2 ± 0.9	0.868 ± 0.021	14.5 ± 1.4	2.611 ± 0.034	100.1 ± 26.7	6.51 ± 0.15	18.93 ± 0.07	21.81 ± 0.05	2.43
9/6	00:24-00:46	14.8 ± 0.6	0.940 ± 0.017	12.1 ± 1.5	2.578 ± 0.043	88.1 ± 26.9	6.62 ± 0.16	18.78 ± 0.12	21.73 ± 0.06	2.49
	02:02-02:12	16.8 ± 1.0	0.867 ± 0.021	13.3 ± 1.5	2.591 ± 0.038	107.6 ± 28.1	6.50 ± 0.14	18.93 ± 0.08	21.81 ± 0.05	1.69
	02:12-02:13	16.9 ± 1.1	0.863 ± 0.023	13.7 ± 0.2	2.613 ± 0.063	110.5 ± 45.5	6.41 ± 0.22	18.91 ± 0.17	21.80 ± 0.06	1.08
	02:14-02:17	16.6 ± 1.1	0.857 ± 0.026	17.0 ± 2.4	2.682 ± 0.052	94.2 ± 33.0	6.36 ± 0.19	18.89 ± 0.12	21.86 ± 0.06	1.61
	02:18-02:24	17.1 ± 1.1	5.847 ± 0.024	16.5 ± 2.0	2.679 ± 0.043	104.3 ± 30.9	6.42 ± 0.16	18.96 ± 0.09	21.86 ± 0.05	2.24
	03:40-04:03	15.3 ± 0.7	0.922 ± 0.018	12.5 ± 1.6	2.590 ± 0.043	92.3 ± 26.7	6.59 ± 0.15	18.79 ± 0.12	21.76 ± 0.06	2.42
	05:18-05:41	15.7 ± 0.8	0.905 ± 0.019	12.3 ± 1.4	2.578 ± 0.040	95.8 ± 27.2	6.55 ± 0.15	18.85 ± 0.10	21.76 ± 0.06	1.61
	06:54-07:18	14.6 ± 0.7	0.940 ± 0.018	14.5 ± 1.9	2.656 ± 0.040	86.6 ± 26.3	6.65 ± 0.16	18.79 ± 0.10	21.80 ± 0.05	1.96
	10:08-10:24	14.3 ± 0.8	0.891 ± 0.023	17.8 ± 2.6	2.808 ± 0.054	105.0 ± 30.2	6.45 ± 0.15	18.89 ± 0.10	21.91 ± 0.05	1.08
	17:42-17:47	15.9 ± 0.8	0.906 ± 0.022	17.6 ± 2.8	2.749 ± 0.057	90.1 ± 30.4	6.48 ± 0.12	18.88 ± 0.12	21.89 ± 0.05	1.38
	18:23-18:44	15.1 ± 0.7	0.917 ± 0.020	17.0 ± 2.6	2.766 ± 0.054	83.8 ± 26.4	6.54 ± 0.17	18.86 ± 0.10	21.86 ± 0.06	1.22
	19:38-19:41	16.7 ± 0.9	0.891 ± 0.022	15.4 ± 3.1	2.775 ± 0.073	106.7 ± 34.6	6.44 ± 0.17	18.92 ± 0.13	21.87 ± 0.06	1.39
	20:00-20:23	16.8 ± 0.4	0.902 ± 0.006	11.4 ± 4.7	2.730 ± 0.015	116.8 ± 28.4	6.58 ± 0.13	18.84 ± 0.08	21.79 ± 0.03	1.89
	21:36-21:59	16.8 ± 0.6	0.907 ± 0.013	9.14 ± 1.5	2.723 ± 0.059	99.0 ± 27.4	6.65 ± 0.14	18.83 ± 0.12	21.74 ± 0.06	2.66
	22:53-23:13	17.3 ± 0.5	0.897 ± 0.011	10.7 ± 1.2	2.789 ± 0.040	91.5 ± 27.2	6.64 ± 0.15	18.85 ± 0.10	21.80 ± 0.04	1.99
9/7	00:33-00:35	18.8 ± 0.9	0.866 ± 0.018	12.7 ± 4.0	2.927 ± 0.117	108.9 ± 37.8	6.56 ± 0.19	19.07 ± 0.14	21.86 ± 0.08	1.00
	00:35-00:50	17.4 ± 0.6	0.899 ± 0.013	7.93 ± 1.6	2.738 ± 0.067	78.2 ± 26.9	6.66 ± 0.18	18.96 ± 0.10	21.74 ± 0.06	1.76
	02:07-02:28	19.7 ± 0.6	0.871 ± 0.011	2.96 ± 0.7	2.471 ± 0.077	83.5 ± 28.9	6.67 ± 0.19	18.70 ± 0.20	21.69 ± 0.06	1.76
	03:45-03:46	21.6 ± 0.2	0.822 ± 0.003	8.05 ± 0.4	2.943 ± 0.026	188.6 ± 55.1	6.19 ± 0.17	18.84 ± 0.28	21.88 ± 0.02	0.88
	03:50-04:08	20.3 ± 0.7	0.848 ± 0.012	3.72 ± 0.9	2.616 ± 0.084	83.0 ± 35.5	6.44 ± 0.22	18.98 ± 0.12	21.76 ± 0.05	0.94
	05:21-05:45	19.7 ± 0.5	0.860 ± 0.008	2.60 ± 0.4	2.494 ± 0.056	82.2 ± 29.4	6.65 ± 0.19	18.86 ± 0.12	21.71 ± 0.04	1.23
	06:57-07:23	18.9 ± 0.7	0.864 ± 0.012	3.12 ± 0.7	2.496 ± 0.075	86.6 ± 30.4	6.56 ± 0.18	18.82 ± 0.15	21.69 ± 0.06	1.54
	08:35-09:02	20.6 ± 0.2	0.838 ± 0.002	4.67 ± 0.9	2.688 ± 0.008	111.1 ± 26.7	6.37 ± 0.14	18.99 ± 0.06	21.81 ± 0.02	2.45
	10:15-10:27	20.2 ± 0.8	0.845 ± 0.014	4.03 ± 1.4	2.682 ± 0.129	119.2 ± 36.8	6.46 ± 0.16	18.96 ± 0.16	21.79 ± 0.06	1.05

NOTE.—The edge energy is fixed at 8.8 keV (MPC2 data).

higher than the innermost temperature (kT_{in}) of the disk. The emitting area (S_{bb}) of these photons is about 1–2 times larger than a neutron star surface but small enough to exist within the innermost radius of the accretion disk. The temperature kT_e and the Thomson scattering depth τ of the Compton cloud are about 25–40 keV and 0.5–0.8, respectively, which are equivalent to the case that the y-parameter of the Compton scattering is about 0.14–0.17 and kT_e is larger than about 30 keV. The column density of the ionized iron atoms $N(Fe^{+24})$, which causes the 8.8 keV K-edge absorption, is $10^{18.2-18.9}$ cm^{-2}, which corresponds to the column density of $N_H = 10^{22.6-23.3}$ cm^{-2} if we assume the cosmic abundance of iron. These ionized iron atoms may be due to the ionized circumstellar gas around GX 339−4.

The ratio of the X-ray photon number of the Comptonized blackbody component to the total X-ray photon number (1–30 keV) is about 0.1–0.2, and the corresponding ratio of the energy flux is about 0.13–0.4.

TABLE 2A

BEST-FIT PARAMETERS OF THE MODEL CONSISTING OF A DISK BLACKBODY AND A COMPTONIZED BLACKBODY (MPC2 DATA)

Time	Disk Black Body $R_{in}(\cos(i))^{0.5}$ (D/4kpc)km	kT_{in} (keV)	Comptonized-Black Body S_{bb} (D/4kpc)²πm²	kT_{bb} (keV)	kT_e (keV)	τ	Equ.W. (eV)	E_{Fe} (keV)	$Log(N_{Fe})$ (cm⁻²)	$Log(N_H)$ (cm⁻²)	red. χ^2 (dof=36)	Intensity (1-37keV)(dens)	Energy (1-37keV) 10⁻⁹erg/sec/4000cm²	C.B.Energy Total Energy (1-37keV)	C.B.Photon Total Photon (1-37keV)	State
9/4 01:56-02:16	29.1±0.9	0.729±0.008	2900±100	0.965±0.006	28.7±1.0	0.69±1.0	84±26	6.51±0.16	18.67±0.12	21.74±0.04	1.13	8486	1.25	0.35	0.18	F
03:34-03:54	27.8±0.9	0.749±0.007	2300±80	0.994±0.007	28.2±1.1	0.71±0.03	84±25	6.45±0.16	18.71±0.12	21.74±0.11	1.57	8336	1.22	0.32	0.17	F
05:13-05:33	28.2±0.8	0.748±0.007	2190±80	0.978±0.007	29.6±1.2	0.65±0.03	79±26	6.46±0.18	18.73±0.10	21.75±0.04	1.17	8168	1.21	0.29	0.16	H
06:49-07:10	26.6±2.8	0.766±0.037	2200±710	0.975±0.057	25.5±2.6	0.78±0.13	90±27	6.40±0.16	18.84±0.11	21.72±0.07	1.44	8153	1.18	0.29	0.17	H
08:25-08:38	27.2±0.8	0.755±0.008	2210±90	0.991±0.007	27.7±1.2	0.72±0.04	76±26	6.43±0.18	18.68±0.13	21.73±0.04	1.33	8176	1.20	0.31	0.19	F
08:38-08:49	29.0±0.9	0.730±0.008	2570±100	0.956±0.007	30.1±1.4	0.63±0.03	86±27	6.44±0.17	18.71±0.13	21.75±0.04	0.95	8040	1.19	0.32	0.18	F
9/5 19:58-20:18	29.7±7.3	0.716±0.007	2256±630	1.007±0.057	28.8±2.5	0.83±0.12	90±29	6.48±0.17	18.64±0.15	21.71±0.08	1.17	7758.	1.16	0.35	0.19	E
21:20-21:40	29.7±7.3	0.716±0.007	2301±77	1.003±0.007	28.6±1.1	0.83±0.03	91±28	6.38±0.16	18.74±0.10	21.72±0.04	1.44	7798	1.18	0.34	0.17	E
21:39-21:43	28.6±6.9	0.730±0.008	2105±101	1.012±0.010	27.0±1.9	0.88±0.06	86±33	6.42±0.20	18.75±0.14	21.71±0.04	1.26	7765	1.16	0.33	0.18	E
22:46-23:30	28.5±1.0	0.727±0.018	2192±217	1.019±0.020	26.3±1.7	0.93±0.07	87±28	6.44±0.17	18.79±0.11	21.71±0.07	1.52	7748	1.17	0.34	0.21	E
9/6 00:24-00:46	28.4±1.0	0.734±0.019	2620±267	0.987±0.018	29.3±1.8	0.74±0.06	80±29	6.44±0.19	18.72±0.13	21.71±0.07	1.41	8380	1.23	0.35	0.18	B
02:02-02:12	28.1±6.8	0.732±0.008	2203±83	1.008±0.008	28.0±1.3	0.87±0.04	91±28	6.47±0.17	18.74±0.11	21.71±0.04	0.96	7723	1.16	0.34	0.18	E
02:12-02:13	27.9±0.4	0.733±0.003	1753±31	1.048±0.005	35.3±2.3	0.72±0.04	82±39	6.44±0.29	18.38±0.39	21.67±0.04	0.79	7706	1.15	0.34	0.18	E
02:14-02:17	29.6±15	0.715±0.050	2098±815	1.026±0.077	29.6±4.1	0.79±0.15	74±39	6.35±0.27	18.53±0.27	21.73±0.10	1.12	7788	1.17	0.35	0.19	E
02:18-02:24	30.2±7.5	0.708±0.008	2350±97	1.000±0.008	27.4±1.5	0.85±0.05	82±31	6.41±0.20	18.75±0.27	21.75±0.04	1.65	7672	1.17	0.35	0.19	E
03:40-04:03	29.1±7.1	0.728±0.007	2542±85	0.989±0.006	28.9±1.0	0.76±0.03	82±27	6.42±0.18	18.70±0.11	21.74±0.04	1.33	8229	1.23	0.35	0.19	B
05:18-05:41	28.4±4.1	0.730±0.003	2539±27	0.984±0.002	28.1±0.4	0.82±0.01	86±23	6.42±0.15	18.74±0.06	21.72±0.03	0.77	7973	1.19	0.35	0.23	B→E
06:54-07:18	28.2±1.3	0.737±0.042	2571±714	0.993±0.052	27.7±2.2	0.76±0.10	80±29	6.51±0.19	18.71±0.13	21.73±0.08	1.01	8370	1.23	0.25	0.20	B→A
10:08-10:24	25.9±3.7	0.736±0.003	2000±27	1.002±0.003	26.9±0.7	0.78±0.02	94±25	6.43±0.15	18.68±0.10	21.71±0.03	0.78	7160	1.01	0.34	0.19	A
17:42-17:47	27.4±0.3	0.745±0.003	2330±40	0.999±0.003	28.8±0.7	0.73±0.02	70±23	6.45±0.19	18.65±0.11	21.73±0.03	0.95	8099	1.19	0.34	0.19	A
18:23-18:44	26.4±1.7	0.754±0.020	2180±250	1.003±0.020	27.5±2.5	0.74±0.07	74±26	6.48±0.20	18.71±0.20	21.69±0.07	0.71	7997	1.16	0.33	0.19	A
19:38-19:41	28.2±0.3	0.737±0.003	2000±40	0.998±0.003	33.1±1.2	0.61±0.02	77±25	6.42±0.18	18.58±0.17	21.76±0.02	0.81	7755	1.16	0.31	0.18	A
20:00-20:23	26.6±0.2	0.757±0.002	1960±20	0.976±0.002	30.3±0.5	0.64±0.01	92±21	6.50±0.13	18.66±0.09	21.71±0.01	1.00	7649	1.11	0.28	0.16	G
21:36-21:59	26.8±0.2	0.756±0.002	1720±20	0.977±0.002	31.0±0.6	0.59±0.01	89±21	6.48±0.13	18.76±0.07	21.73±0.02	1.58	7417	1.09	0.26	0.14	G
22:53-23:13	26.3±0.2	0.763±0.002	1700±20	0.975±0.002	28.8±0.5	0.63±0.01	82±21	6.49±0.15	18.76±0.07	21.74±0.02	1.36	7382	1.08	0.33	0.14	G
9/7 00:33-00:35	26.5±1.7	0.763±0.020	1390±340	0.983±0.037	35.6±12.8	0.51±0.15	91±39	6.54±0.20	18.88±0.28	21.73±0.06	0.74	7192	1.06	0.22	0.13	G
00:35-00:50	27.6±2.7	0.746±0.039	1700±660	0.955±0.060	34.5±3.8	0.49±0.11	71±28	6.45±0.20	18.87±0.11	21.77±0.07	0.77	7198	1.07	0.24	0.14	G
02:07-02:28	26.4±0.2	0.772±0.002	1140±20	0.955±0.003	39.8±1.1	0.51±0.01	80±22	6.44±0.15	18.68±0.11	21.79±0.02	0.88	6895	1.04	0.17	0.09	G
03:45-03:46	25.1±0.2	0.779±0.003	900±50	0.957±0.009	36.7±4.8	0.53±0.06	132±45	6.24±0.19	18.19±0.99	21.77±0.03	0.79	6546	0.95	0.14	0.08	G
03:50-04:08	25.3±2.1	0.771±0.035	1360±730	0.904±0.067	36.0±11.2	0.51±0.24	63±28	6.35±0.24	18.89±0.14	21.76±0.06	0.76	6590	0.96	0.17	0.10	G
05:21-05:45	24.2±0.5	0.789±0.006	940±60	0.945±0.010	36.6±2.8	0.57±0.04	77±27	6.51±0.19	18.81±0.13	21.75±0.03	0.92	6520	0.94	0.15	0.08	G
06:57-07:23	24.7±0.2	0.772±0.002	1300±20	0.921±0.003	34.6±0.8	0.58±0.01	81±22	6.40±0.15	18.81±0.08	21.74±0.02	0.97	6426	0.93	0.18	0.10	G
08:35-09:02	24.7±0.2	0.777±0.002	1100±20	0.935±0.003	37.3±1.1	0.53±0.01	77±22	6.37±0.16	18.73±0.10	21.76±0.02	1.56	6425	0.93	0.16	0.14	G
10:15-10:27	23.0±1.1	0.804±0.016	830±220	0.948±0.041	29.6±9.0	0.70±0.20	98±31	6.46±0.18	18.85±0.24	21.74±0.05	1.10	6322	0.91	0.13	0.14	G

TABLE 2B

BEST-FIT PARAMETERS OF THE MODEL CONSISTING OF A DISK BLACKBODY AND A COMPTONIZED BLACKBODY FOR A SPECTRUM OF EACH POWER SPECTRAL STATE

PARAMETER	POWER SPECTRAL STATE							
	A	B	C	D	E	F	G	H
Time	Sep 6, 13:23–15:27	Sep 3, 14:50–15:15	Sep 5, 14:58–17:04	Sep 5, 13:24–13:53	Sep 5, 19:58–20:18	Sep 4, 01:56–02:16	Sep 6, 20:00–20:23	Sep 4, 05:13–05:33
Disk Blackbody:								
$R_{in}[\cos(i)]^{0.5}$ (D/4 kpc) km	27.0 ± 2.0	27.4 ± 1.9	27.7 ± 1.7	28.5 ± 1.8	29.7 ± 7.3	29.1 ± 0.9	26.6 ± 0.2	28.2 ± 0.8
kT_{in} (keV)	0.745 ± 0.025	0.727 ± 0.026	0.727 ± 0.026	0.690 ± 0.026	0.716 ± 0.007	0.729 ± 0.008	0.757 ± 0.002	0.748 ± 0.007
Comptonized Blackbody:								
S_{bb} (D/4 kpc)^2 km^2	2070 ± 410	2300 ± 460	1780 ± 330	2080 ± 380	2256 ± 630	2900 ± 100	1960 ± 20	2190 ± 80
kT_{bb} (keV)	1.01 ± 0.04	0.98 ± 0.04	1.06 ± 0.04	1.03 ± 0.04	1.007 ± 0.057	0.965 ± 0.006	0.976 ± 0.002	0.978 ± 0.007
kT_e (keV)	31.0 ± 3.4	29.5 ± 3.2	28.0 ± 2.8	27.5 ± 2.8	28.8 ± 2.5	28.7 ± 1.0	30.3 ± 0.5	29.6 ± 1.2
τ	0.69 ± 0.08	0.74 ± 0.10	0.91 ± 0.11	0.94 ± 0.10	0.83 ± 0.12	0.69 ± 1.0	0.64 ± 0.01	0.65 ± 0.03
Iron Line:								
I_{Fe} or EW (counts s^{-1} or eV)	23 (Fixed)	23 (Fixed)	23 (Fixed)	23 (Fixed)	90 ± 29 eV	84 ± 26 eV	92 ± 21 eV	79 ± 26 eV
E_{Fe} (keV)	6.45 (Fixed)	6.45 (Fixed)	6.45 (Fixed)	6.45 (Fixed)	6.48 ± 0.17	6.51 ± 0.16	6.50 ± 0.13	6.46 ± 0.18
log (N_{Fe}) (cm^{-2})	18.7 (Fixed)	18.7 (Fixed)	18.7 (Fixed)	18.7 (Fixed)	18.64 ± 0.15	18.67 ± 0.12	18.66 ± 0.09	18.73 ± 0.10
log (N_H) (cm^{-2})	21.7 (Fixed)	21.7 (Fixed)	21.7 (Fixed)	21.7 (Fixed)	21.71 ± 0.08	21.74 ± 0.04	21.71 ± 0.01	21.75 ± 0.04
Reduced χ^2	0.24	0.17	0.74	0.60	1.17	1.13	1.00	1.17
Intensity (1–37 keV) (counts s^{-1})	7850	7520	6890	6620	7558	8486	7649	8166
Energy (1–37 keV) (10^{-4} ergs s^{-1} 4000 cm^{-2})	1.16	1.09	1.05	1.00	1.16	1.25	1.11	1.21
(Comptonized blackbody energy)/(Total energy)	0.33	0.35	0.36	0.40	0.35	0.35	0.28	0.29
(Comptonized blackbody photon)/(Total photon)	0.18	0.20	0.19	0.21	0.19	0.18	0.16	0.16

793

The energy of the iron emission line is about 6.4–6.5 keV, which is a little lower than the value of 6.7 keV expected from the helium-like iron. However, we could get acceptable fits even if we fixed the energy of the line to 6.7 keV. As the equivalent width of the line is about 60–100 eV, a slight change in the energy spectrum of the continuum cloud change the energy of the line.

Hereafter, we will adopt the model in which the X-ray energy spectrum consists of a disk blackbody (low-energy) component and a Comptonized blackbody component (high-energy tail).

2.3. Power Spectral Density Functions: QPOs, Low-Frequency Noise (LF Noise), Very Low Frequency Noise (VLF Noise), and Power Spectral States

LAC observations in the MPC-3 mode in high bit rate have a time resolution of 7.8 ms, and the power spectral density functions were calculated from these data. We found that there were four states which could be resolved, and we named them power spectral states A, B, C, and D. Some examples of these power spectra are shown in Figure 4. The vertical axis is a normalized power spectral density function, which is the power spectral density function normalized to the squared mean
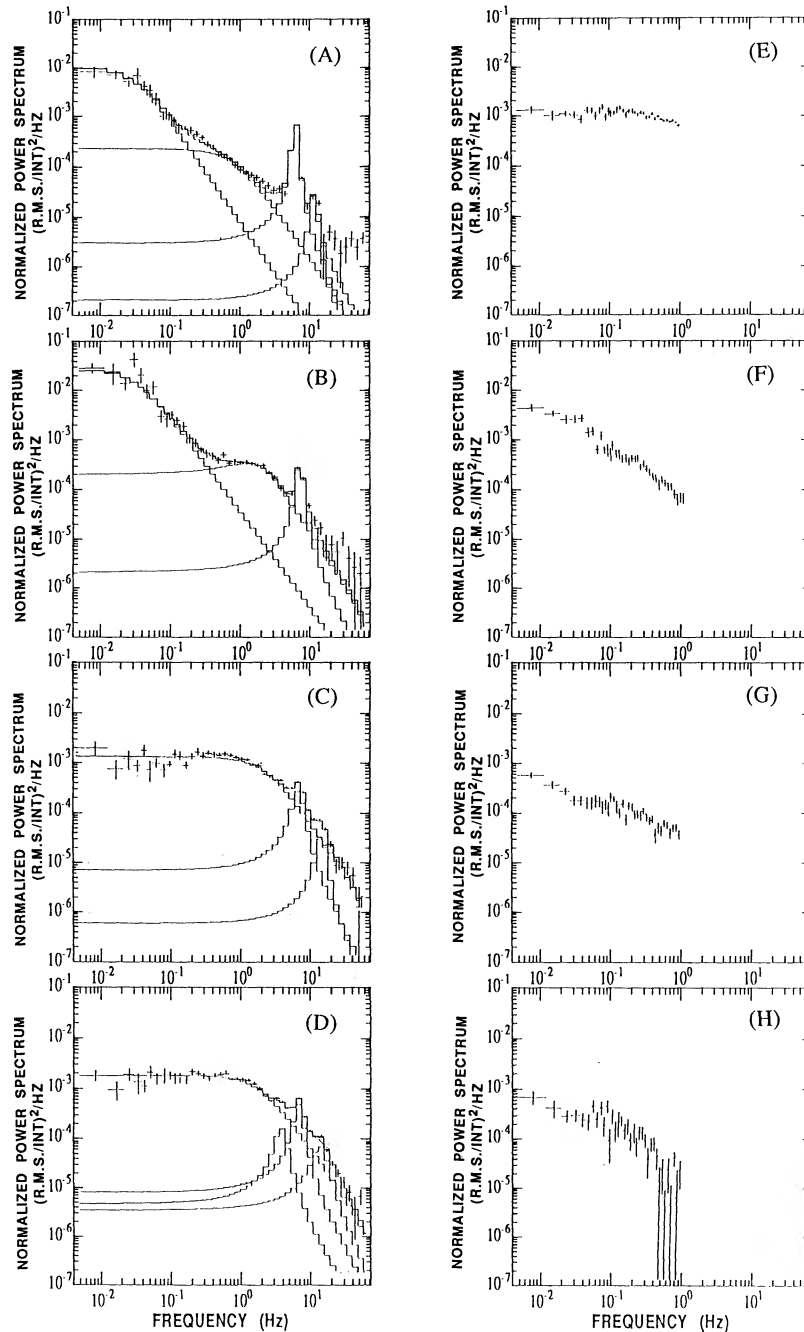

FIG. 4.—Normalized power spectral density functions of various power spectral states. (A) September 6, 13:23–15:27; (B) September 3, 14:50–15:15; (C) September 5, 14:58–17:04; (D) September 5, 13:24–13:53; (E) September 5, 19:58–20:18; (F) September 4, 01:56–02:16; (G) September 6, 20:00–20:23; (H) September 4, 05:13–05:33.

intensity and is suitable to see the variable amplitude relative to the mean intensity.[3] There are quasi-periodic oscillations (QPOs) of about 6 Hz in all of them. In the power spectral states of A and B, the QPOs have a sharp peak, and both states have flat noise at frequencies below 0.06 Hz. We call this noise a very low frequency noise (VLF noise). This VLF noise corresponds to flip-flop–type time variations in state B and dip-type time variations in state A (see § 2.5). There is also a low-frequency noise (LF noise) in states A and B, which is flat at the frequencies below about 1–2 Hz. The power spectral state B has more noise than state A at frequencies below 10 Hz.

There is no VLF noise in the power spectral states C and D, and the low-frequency noise (LF noise) is dominant. The LF noise is similar in both power spectral states C and D, and the QPO peaks are somewhat broader in these power spectral states that in the power spectral states A and B. The power spectral density functions of the states C and D are very similar, though in the power spectral state C there are oscillations at about double frequencies of the QPOs, and in the power spectral state D there are oscillations at about half and double frequencies of the QPOs.

There are data which were observed in MPC-2 mode in medium bit rate whose time resolution are 0.5 s. We calculated the normalized power spectral density function from these data. On the basis of the information below 1 Hz, we concluded that there were four power spectral states E, F, G, and H; they are shown in Figure 4. Although we have no information about QPOs in these power spectral states due to the poor time resolution of the data, we found that the power spectral state E was similar to the power spectral states of C and D. The shape of the power spectral density function of the power spectral state F is similar to that of the power spectral state A. Shapes of the power spectral states of G and H are intermediate between A (B) and C (D), and the normalized power spectral density functions of the states G and H are lower than those of all other states.

---

[3] There is another normalization method by Leahy et al. (1983), which normalizes the power spectral density function to the mean photon number. This normalization is suitable to derive statistical significance of the variation.

These eight power spectral states are shown in the light curves in Figure 2 and Table 2.

In conclusion, the shapes of the power spectral density functions are of three different types. The first is the type of the states A, B, and F, where the VLF noise is predominant; the second is that of the states C, D, and E, where the LF noise is predominant; and the third is that of the states G and H, which has an intermediate shape of power spectral density function between the first and the second shapes and also has the lowest normalized power spectral density function. We found that the values of the normalized power spectral density function have a tendency to decrease with the decrease of the Comptonized blackbody component.

2.4. Power Spectral States and Energy Spectral Branches

We made an X-ray hardness ratio (color)–intensity (count rate) diagram; $I(9.3–37.1\ \mathrm{keV})/I(4.6–9.3\ \mathrm{keV})$ versus $I(1.2–37.1\ \mathrm{keV})$ and a color-color diagram; $I(9.3–37.1\ \mathrm{keV})/I(4.6–9.3\ \mathrm{keV})$ versus $I(4.6–9.3\ \mathrm{keV})/I(1.2–4.6\ \mathrm{keV})$ to investigate the energy spectral variations of the source, which are shown in Figure 5.

The eight power spectral states have their restricted regions in the color-intensity and the color-color diagram. One can find that the power spectral states of C, D, and E are on a branch where the hardness ratio decreases as the X-ray count rate increases, and the power spectral states of G and H are on a branch where the hardness ratio increases as the X-ray count rate increases. We call these a "hardness ratio decreasing (with the X-ray flux) branch" and a "hardness ratio increasing branch," respectively. The power spectral states A, B, and F are on the crossing region of these two branches.

As mentioned in § 2.3, the power spectral density functions can be divided into three different types. These three types have different regions in the color-intensity and the color-color diagram; the two branches and their crossing regions as shown in Figure 5. Similar power spectral states have their positions in similar part of the energy spectral branches.

The energy spectra of A and B are very similar to each other, and those of C and D are also very similar to each other. A comparison between the energy spectra of the two types (the power spectral state A and D) is shown in Figure 6a. The differences between these two groups are as follows. The
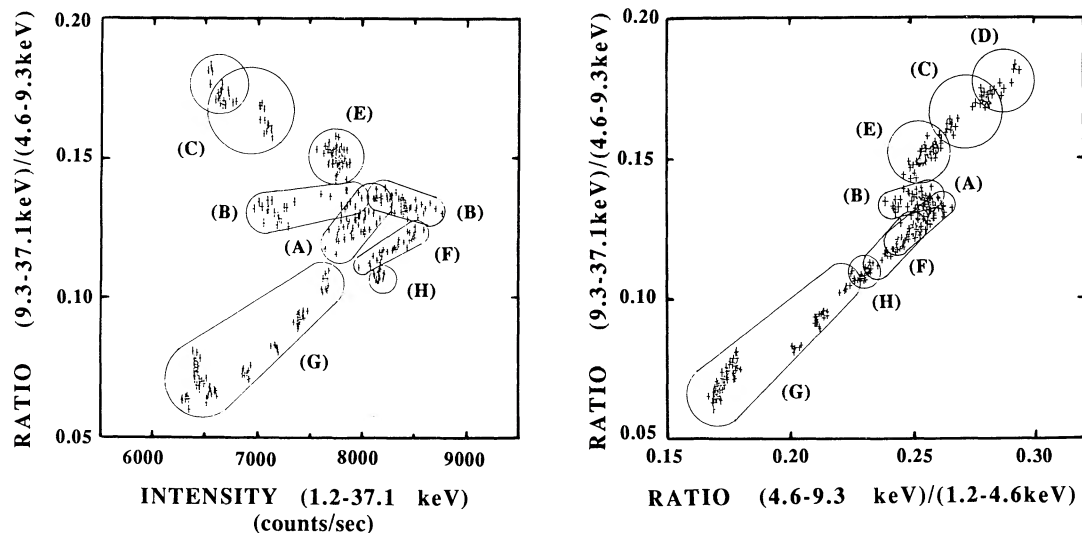

FIG. 5.—A color-intensity and a color-color diagram. The power spectral states are also shown.
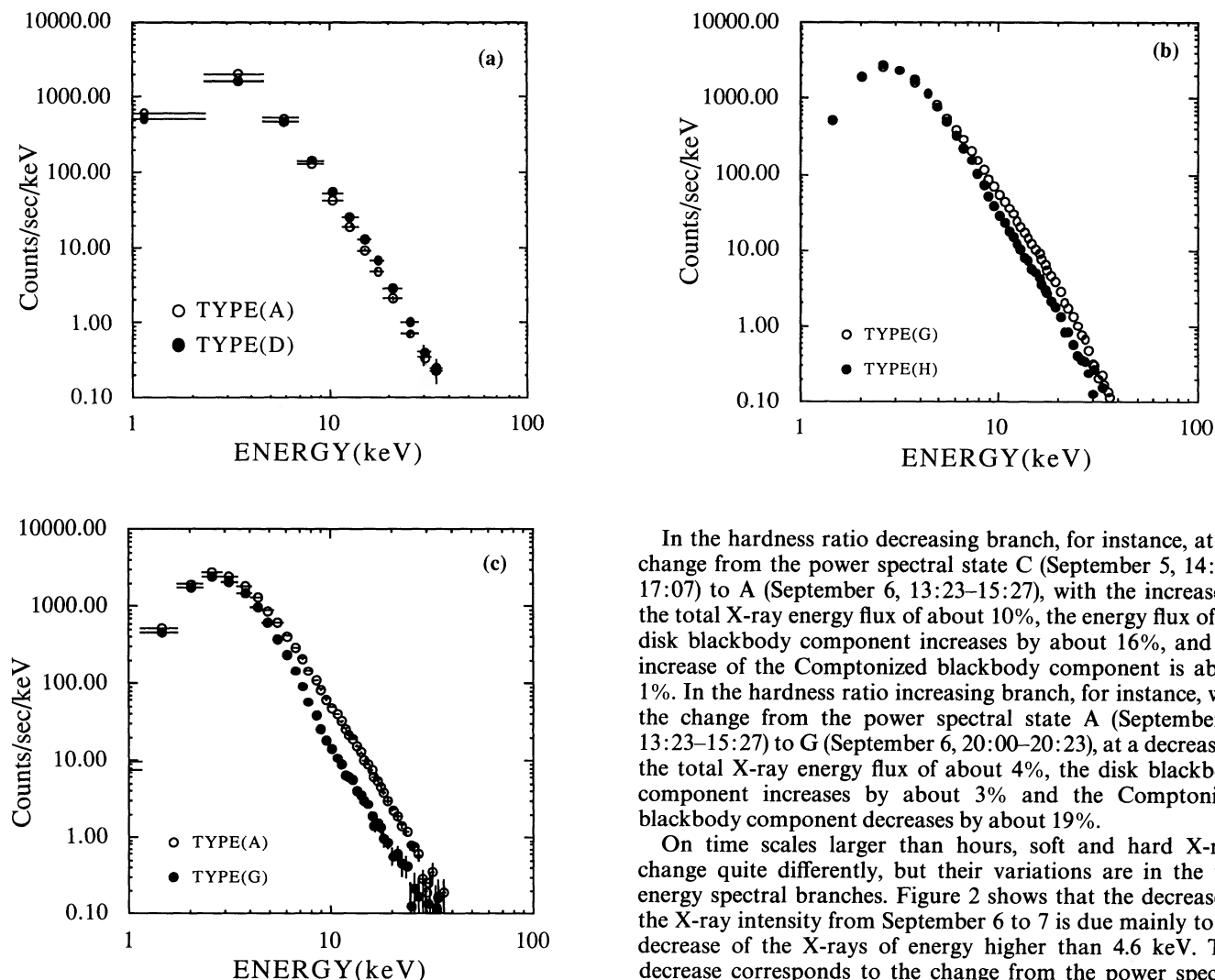
FIG. 6.—Energy spectra of different power spectral states. (a) (A) September 6, 13:23–15:27; (D) September 5, 13:24–13:53. (b) (G) September 6, 21:36–21:59; (H) September 4, 01:56–02:15. (c) (A) September 6, 17:42–17:47; (G) September 7, 10:16–10:27.

energy spectra of C and D are harder than those of A and B; the energy spectra of C and D have smaller fluxes at the energies <7 keV and have larger fluxes at >7 keV than those of A and B. The energy spectra of the power spectral states E, F, G, and H are similar, and their difference is mainly in their high-energy part. The differences between the power spectral states G and H are shown in Figure 6b. The difference between the power spectral state A and G is also in their high-energy part as shown in Figure 6c.

These differences of the energy spectra can be seen clearly by fitting the energy spectra with the disk blackbody and Comptonized blackbody spectrum model described in § 2.2. The results are shown in Table 2B. From these, we can find that in the hardness ratio decreasing branch, the disk blackbody component is the main cause of the change of the X-ray flux. On the other hand, in the hardness ratio increasing branch, the Comptonized blackbody component is the main cause of the change.

In the hardness ratio decreasing branch, for instance, at the change from the power spectral state C (September 5, 14:58–17:07) to A (September 6, 13:23–15:27), with the increase of the total X-ray energy flux of about 10%, the energy flux of the disk blackbody component increases by about 16%, and the increase of the Comptonized blackbody component is about 1%. In the hardness ratio increasing branch, for instance, with the change from the power spectral state A (September 6, 13:23–15:27) to G (September 6, 20:00–20:23), at a decrease of the total X-ray energy flux of about 4%, the disk blackbody component increases by about 3% and the Comptonized blackbody component decreases by about 19%.

On time scales larger than hours, soft and hard X-rays change quite differently, but their variations are in the two energy spectral branches. Figure 2 shows that the decrease of the X-ray intensity from September 6 to 7 is due mainly to the decrease of the X-rays of energy higher than 4.6 keV. This decrease corresponds to the change from the power spectral state A to G in the hardness ratio increasing branch, where the Comptonized blackbody component decreases largely during this time.

However, on September 5, from 12:00 to 10:00 the X-rays with energies <4.6 keV increase in spite of the decrease of the X-rays with energies >9.3 keV. This change accompanies the change in the power spectral state from C (D) to E, which corresponds to the change in the hardness ratio decreasing branch, and the disk blackbody component increases.

We also remarked that the change always passed through the crossing region between the two branches; direct changes between the hardness ratio increasing branch and the hardness ratio decreasing branch without passing through the crossing region were not observed.

Thus, though the disk blackbody component and the Comptonized blackbody component showed almost independent long-term variations on time scales of several hours, these variations were always in the two branches and their crossing region.

2.5. Dip- and Flip-Flop–Type Intensity Variations

In the power spectral state A, dip-type intensity variations were frequently observed. They occur at a frequency of about one per 4 minutes and their durations are about 10–20 s. In the power spectral state B, longer dips of about 20–60 s were
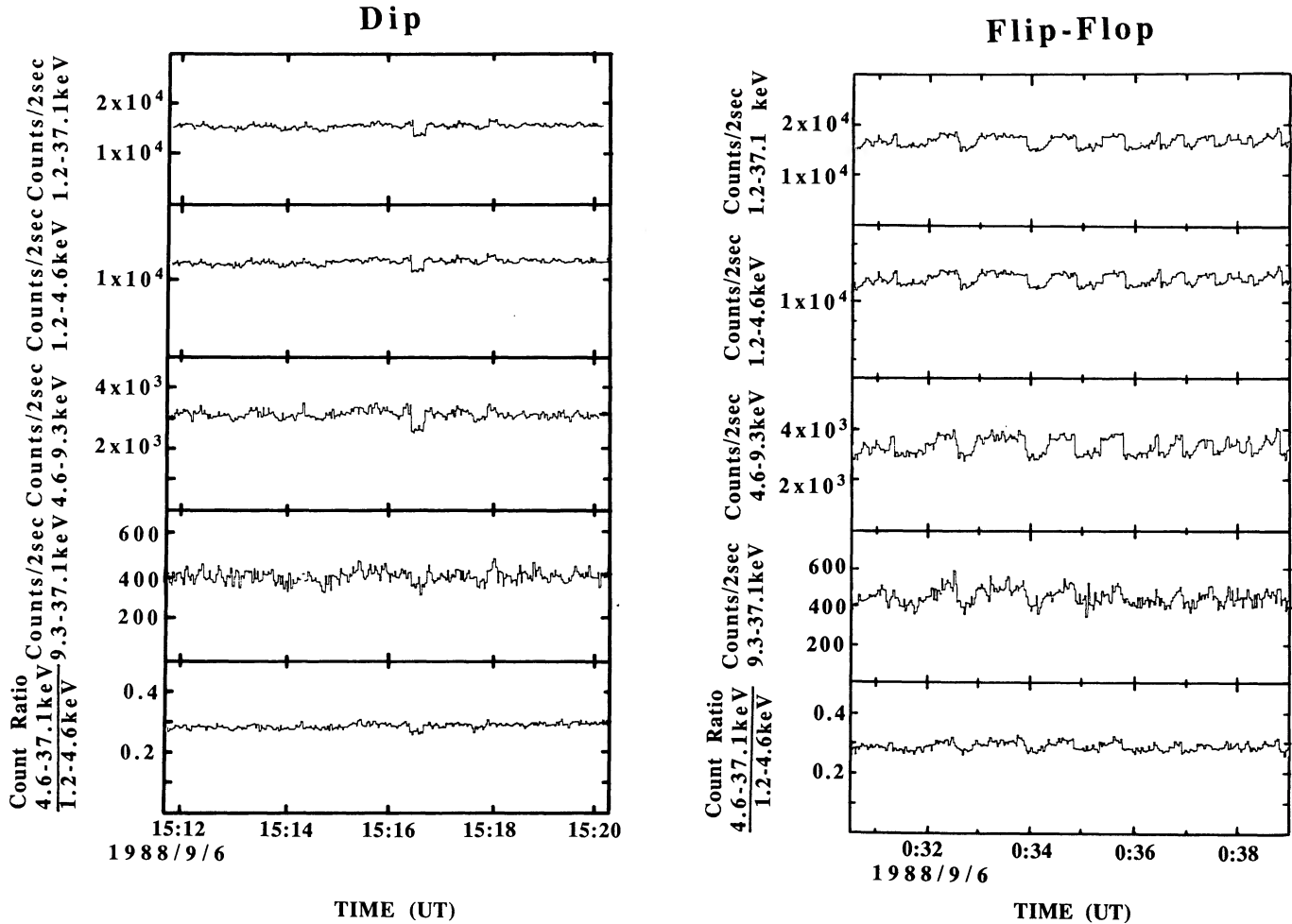
Dip

Flip-Flop

FIG. 7.—Some examples of the dip and flip-flop

observed at a frequency of about one per minute. We call the latter flip-flop–type intensity variations. Some examples of these variations are shown in Figure 7. Usually the decreases of the intensity were about 10%–20% in the energy range of 1.2–37.1 keV within a few tenths of a second.

In both types of intensity variations, the decrease in intensity is more rapid than the increase. The most rapid decrease observed in dip and flip-flop is a 25% intensity decrease in 94 ms.

The power spectral density functions of the high and the low levels of the dip and the flip-flop variations are calculated and shown in Figure 8. The high levels of the dip and the flip-flop variations have power spectra similar to those in the A state, and the power spectra of the low levels are similar to those of the power spectral state C or D. There is some indication of an oscillation near 3 Hz (Fig. 8). Thus the power spectral density functions of the high and low levels are similar to those in the hardness ratio decreasing branch.

The energy spectra of the high and the low level of the flip-flop variations are shown in Figure 9, and these are fitted with the disk blackbody and Comptonized blackbody spectrum model. The results are shown in Table 3. From these we can find that with the change from the low to the high level the energy of the disk blackbody component does not change

appreciably and that the Comptonized blackbody component increases by about 30%. This change is similar to the long-term time variations in the hardness ratio increasing branch, despite the fact that the power spectral states of the low and the high level are in the hardness ratio decreasing branch.

As mentioned in § 2.3, the shape of the power spectral state F is similar to that of state A. We found that the X-ray light curves in the power spectral state F did not show clear dips as in the power spectral state A. However, they showed significant variations with an amplitude of about 10% on time scales of 10–100 s.

2.6. Energy Spectra of QPO, LF Noise, and VLF Noise Components

To get the parameters of the QPO, VLF noise, and LF noise components, the power density spectra were fitted with Lorentzian profiles $L(\omega)$, expressed by

$$L(\omega) = I(\gamma^2/4)/[(\omega - \omega_0)^2 + (\gamma)^2] , \qquad (1)$$

where ω_0 is the central frequency and γ is the FWHM (full width at half-maximum). For the VLF noise and the LF noise component, we fixed the value of ω_0 as zero except for those shown in Table 4. The fitting results are shown in Figure 4 and Table 4.
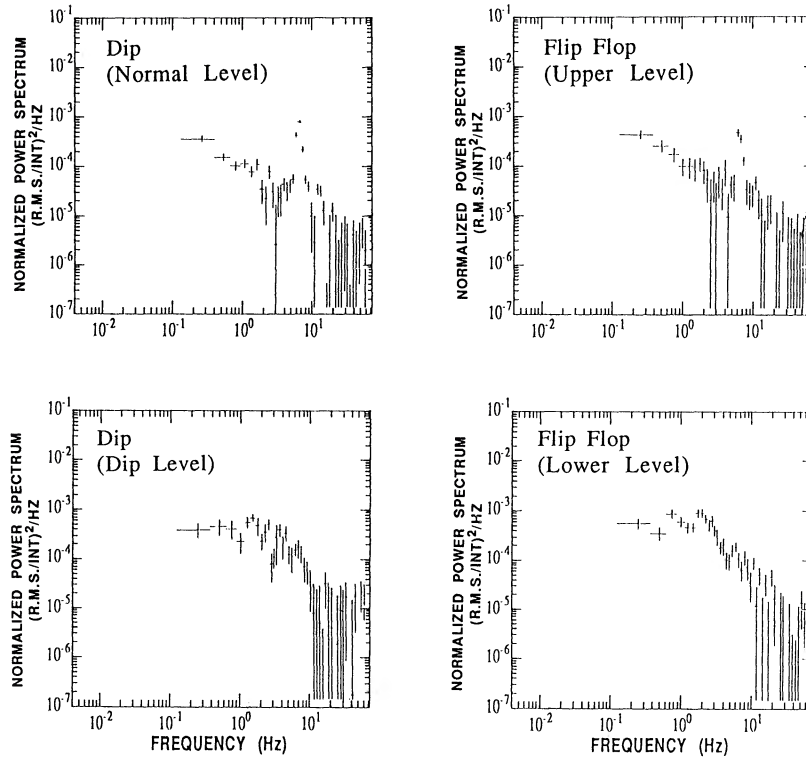
FIG. 8.—Normalized power spectral density functions of the high and the low level of the dip and the flip-flop. Flip-flop (low); September 3, 14:24–15:07; flip-flop (high); September 3, 14:51–15:06; dip (low); September 6, 15:07–15:24; dip (high); September 6, 15:12–15:25.

The energy spectra of the root mean square (rms) amplitude of QPO, LF noise, and VLF noise components are calculated using the method described by Mitsuda (1989) and Dotani (1989), and the results are shown in Figure 10 together with the energy spectrum of the Comptonized blackbody component.

The LF noise component (C, D) has a rms amplitude energy spectrum a little softer than the VLF noise component (A, B), and this component has the rms amplitude energy spectrum similar to the Comptonized blackbody component.
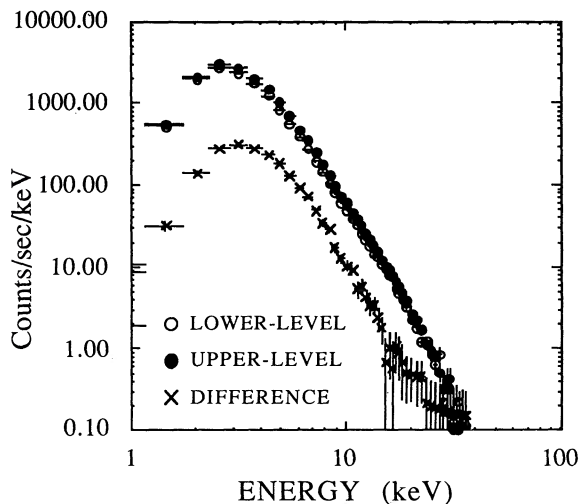

FIG. 9.—Energy spectra of the high and the low level of the flip-flop (September 4, 00:19–00:28).

The rms amplitude energy spectra of the QPO component in the states A, B, and D are similar to or somewhat harder than those of the Comptonized blackbody component. The rms amplitude energy spectrum of the QPOs in state C is harder than those of Comptonized blackbody component.

The amplitudes of the dip, the flip-flop, and the QPOs are quite large. For example, the amplitude of the flip-flop is about 9% of the mean flux at 1.2–4.6 keV and about 14% at 4.6–9.3 keV at 00:32–00:36 on September 6 (UT) as shown in Figure 7. The amplitude of the QPO component is about 20% of the mean flux at 1.2–4.6 keV and about 40% at 4.6–9.3 keV at 15:07 on September 6 (the power spectral state A), which are shown in Figure 11. These amplitudes are larger at higher X-ray energies, which is consistent with the results that the difference of the flux between the high and the low level of the dip and the flip-flop are due to the Comptonized blackbody component and that the QPO component has the rms amplitude energy spectra similar to or harder than that of the Comptonized blackbody component.

2.7. Phase and Time Lags of the Time Variations between Different Energy X-Rays

As the X-ray energy spectrum comprise a very soft (disk blackbody) component and a hard tail (Comptonized blackbody component), and the latter component shows rapid time variation, there should exist some phase lag which may suggest the production process of the hard tail. To investigate this, we calculated the phase lag by means of a similar method described by van der Klis et al. (1987) and Miyamoto et al. (1988) on the data of the time resolution of 7.8 ms (the data of the power spectral states A, B, C, and D), and 128 s data

TABLE 3

BEST-FIT PARAMETERS FOR THE UPPER LEVEL AND LOWER LEVEL OF THE FLIP-FLOP AND OF THE DIPS

Parameter	Upper Level of Flip-Flop	Lower Level of Flip-Flop	Upper Level of Dip	Lower Level of Dip
Time	Sep 3, 14:51–15:07	Sep 3, 14:53–15:06	Sep 6, 15:07–15:24	Sep 6, 15:12–15:23
Disk Blackbody:				
$R_{in}[\cos(i)]^{0.5}\,(D/4\,\mathrm{kpc})$ km	27.9 ± 2.4	28.0 ± 2.0	27.9 ± 2.1	28.2 ± 1.1
kT_{in} (keV)	0.735 ± 0.005	0.728 ± 0.029	0.733 ± 0.030	0.731 ± 0.013
Comptonized Blackbody:				
$S_{bb}\,(D/4\,\mathrm{kpc})^2$ km^2	2900 ± 70	2200 ± 570	2730 ± 600	1440 ± 140
kT_{bb} (keV)	0.975 ± 0.05	0.988 ± 0.049	0.967 ± 0.036	1.060 ± 0.021
kT_e (keV)	27.6 ± 1.1	34.0 ± 5.6	29.5 ± 3.5	33.6 ± 5.4
τ	0.74 ± 0.03	0.72 ± 0.13	0.70 ± 0.01	0.74 ± 0.09
Iron Line:				
I_{Fe} or EW (counts s^{-1} or eV)	23 counts s^{-1} (Fixed)	23 counts s^{-1} (Fixed)	23 counts s^{-1} (Fixed)	23 counts s^{-1} (Fixed)
E_{Fe} (keV)	6.45 (Fixed)	6.45 (Fixed)	6.45 (Fixed)	6.45 (Fixed)
$\log(N_{Fe})$ (cm^{-2})	18.7 (Fixed)	18.7 (Fixed)	18.7 (Fixed)	18.7 (Fixed)
$\log(N_H)$ (cm^{-2})	21.7 (Fixed)	21.7 (Fixed)	21.7 (Fixed)	21.7 (Fixed)
Reduced χ^2	1.33	0.44	0.11	1.19
Intensity (1–37 keV) (counts s^{-1})	8370	7380	7910	7120
Energy (1–37 keV) (10^{-4} ergs s^{-1} 4000 cm^{-2})	1.21	1.10	1.17	1.09
(Comptonized blackbody energy)/(Total energy)	0.38	0.33	0.36	0.30
(Comptonized blackbody photon)/(Total photon)	0.22	0.18	0.21	0.15

segments were used. The energy ranges used were 1.2–2.3, 2.3–4.6, 4.6–9.3, 9.3–13.9, and 13.9–37.1 keV. We could get clear results from the combined data of the power spectral states C and D. The results, i.e., the phase lags and the time lags of the time variations of the various energy X-rays relative to those of the energy range of 2.3–4.6 keV, are shown in Figure 12. From

the data of the power spectral states A and B, we could not get clear results because of their large errors. However, the results are consistent with the result of the power spectral state C and D.

The conclusions of this analysis are as follows.

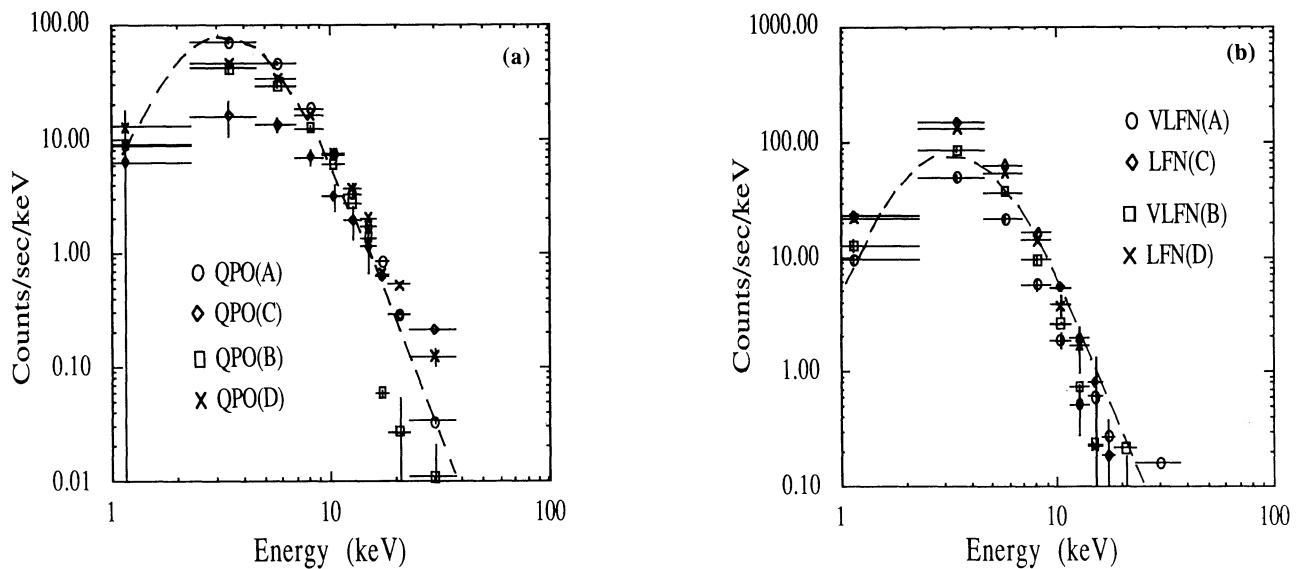1. The time variation in the energy range of 2.3–4.6 keV is

FIG. 10.—Root-mean-squares amplitude energy spectra of the (a) QPO and (b) LF noise and VLF noise. The energy spectrum of the Comptonized blackbody component is shown by a dashed curve. QPO(A): September 6, 13:23–15:27; QPO(B): September 6, 10:26–12:08; QPO(C): September 5, 14:58–17:04; QPO(D): September 5, 13:24–13:53; VLF noise (A): September 6, 13:23–15:27; VLF noise (B): September 6, 10:26–12:08; LF noise (C): September 5, 14:58–17:04; LF noise (D): September 5, 13:24–13:53.

TABLE 4

BEST-FIT PARAMETERS OF A POWER SPECTRUM OF EACH STATE

| PARAMETER	POWER SPECTRAL STATE							
	A	B	C	D	E	F	G	H
Time	Sep 6, 13:23–15:27	Sep 3, 14:50–15:15	Sep 5, 14:58–17:04	Sep 5, 13:24–13:53	Sep 5, 19:58–20:18	Sep 4, 01:56–02:16	Sep 6, 20:00–20:23	Sep 4, 05:13–05:33
VLFN (Lorentzian):								
Relative Amplitude (%)	2.60 ± 0.01	5.78 ± 0.71	...	...	...	0.80 ± 0.18	0.62 ± 0.26	1.65 ± 0.31
Central Frequency (Hz)	0.0 (Fixed)	0.0 (Fixed)	...	...	...	0.0 (Fixed)	0.0 (Fixed)	0.0 (Fixed)
Width (FWHM) (Hz)	0.0556 ± 0.0004	0.0549 ± 0.0084	...	...	...	0.057 ± 0.012	0.030 ± 0.012	0.375 ± 0.072
LFN (Lorentzian):								
Relative Amplitude (%)	2.32 ± 0.01	4.87 ± 0.15	9.31 ± 0.15	9.50 ± 0.26	5.4 ± 0.1	2.74 ± 0.66	2.03 ± 0.36	...
Central Frequency (Hz)	0.001 ± 0.005	1.32 ± 0.14	0.0 (Fixed)	0.0 (Fixed)	0.0 (Fixed)	0.0 (Fixed)	0.0 (Fixed)	...
Width (FWHM) (Hz)	1.44 ± 0.01	3.02 ± 0.33	4.41 ± 0.17	3.79 ± 0.33	2.0 (Fixed)	1.19 ± 0.31	1.73 ± 0.45	...
QPO (Fundamental) (Lorentzian):								
Relative Amplitude (%)	4.72 ± 0.01	3.54 ± 0.16	3.87 ± 0.15	4.75 ± 0.24	...	...	...	...
Central Frequency (Hz)	5.88 ± 0.01	6.54 ± 0.04	6.64 ± 0.09	6.05 ± 0.06	...	...	...	...
Width (FWHM) (Hz)	0.57 ± 0.01	1.08 ± 0.30	2.46 ± 0.30	1.48 ± 0.20	...	...	...	...
QPO (Second Harmonic) (Lorentzian):								
Relative Amplitude (%)	1.38 ± 0.01	...	1.66 ± 0.19	3.04 ± 0.25	...	...	...	...
Central Frequency (Hz)	11.4 ± 0.1	...	13.8 ± 0.5	12.4 ± 0.4	...	...	...	...
Width (FWHM) (Hz)	1.54 ± 0.03	...	3.79 ± 1.52	4.34 ± 1.14	...	...	...	...
QPO (3 Hz) (Lorentzian):								
Relative Amplitude (%)	...	...	...	1.63 ± 0.37	...	...	...	...
Central Frequency (Hz)	...	...	...	3.14 ± 0.13	...	...	...	...
Width (FWHM) (Hz)	...	...	...	0.46 ± 0.48	...	...	...	...
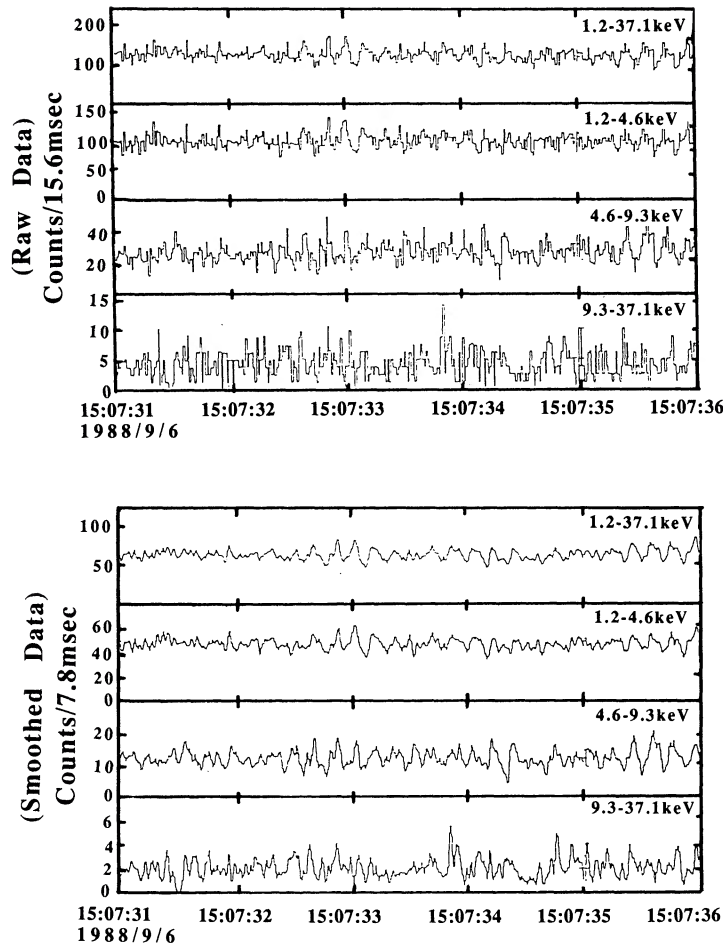
FIG. 11.—Examples of the X-ray light curves which show QPOs (September 6, 15:07:31–15:07:35). The curves in the lower part of the figure show the values smoothed by an average of adjoining five bins with the weights of 1, 2, 3, 2, 1.

most advanced: the time variation of 1.2–2.3 keV X-rays shows a soft lag relative to that of 2.3–4.6 keV X-rays, and the time variations of the X-rays of the energy higher than 4.6 keV shows a hard lag relative to that of 2.3–4.6 keV X-rays. The hard lag is larger for higher energy X-rays.

2. Every phase lag has a peak structure; it has a maximum in the diagram of phase lag versus Fourier period.

3. Every time lag has a flat shoulder at a midslope. This structure corresponds to the peak in the phase lag.

We also calculated the phase lag near the QPO frequencies for the power spectral states A, B, and the joint power spectral state of C and D relative to the time variation of the X-rays of 2.3–4.6 keV, and found that the time variations of the QPO component in the energy range of 2.3–4.6 keV was most advanced, which was similar to the phase lag mentioned in conclusion (1). These phase lags of QPOs in the spectral state A and B are almost similar to those of the neighboring frequencies. But in the joint power spectral state of C and D, in the energy ranges of 9.3–13.9 keV and 13.9–37.1 keV, the phase lags of QPOs relative to the energy range of 2.3–4.6 keV are smaller by a factor of 2–3 than those at its neighboring frequencies. And the phase lags of QPOs in the joint power spectral state C and D are also smaller than those of the QPOs of the power spectral states A and B by a factor of about 1.5–2.0.

3. DISCUSSION

3.1. The Very High State

The state of GX 339−4 observed this time is different from its high state in several ways.

1. The X-ray flux is larger than that of previous observations of the high state by a factor of 2–3.

2. The energy spectrum is slightly different from that of the high state. We fitted the observed X-ray energy spectrum with the model of a disk blackbody and a power law to compare with previous observations though the fittings are not good. The results are shown in Table 1. We found that the temperature (kT_{in}) of the innermost edge of the accretion disk is about 0.9–1.0 keV. The photon index of the power law is about −2.3 to −2.6, which is different from those previously observed in its high state by Makishima et al. (1986) of about −0.9 to −2.1. The index observed by Ilovaisky et al. (1986) was −2.2 ± 0.2.

3. There are very rapid time variations in the X-ray intensity. Previously in the high state, no rapid time variation was observed (Makishima et al. 1986; Ilovaisky et al. 1986). As the rapid time variable component is the hard tail component, there must be a different production process of the hard tail component in this very high state than in the high state.
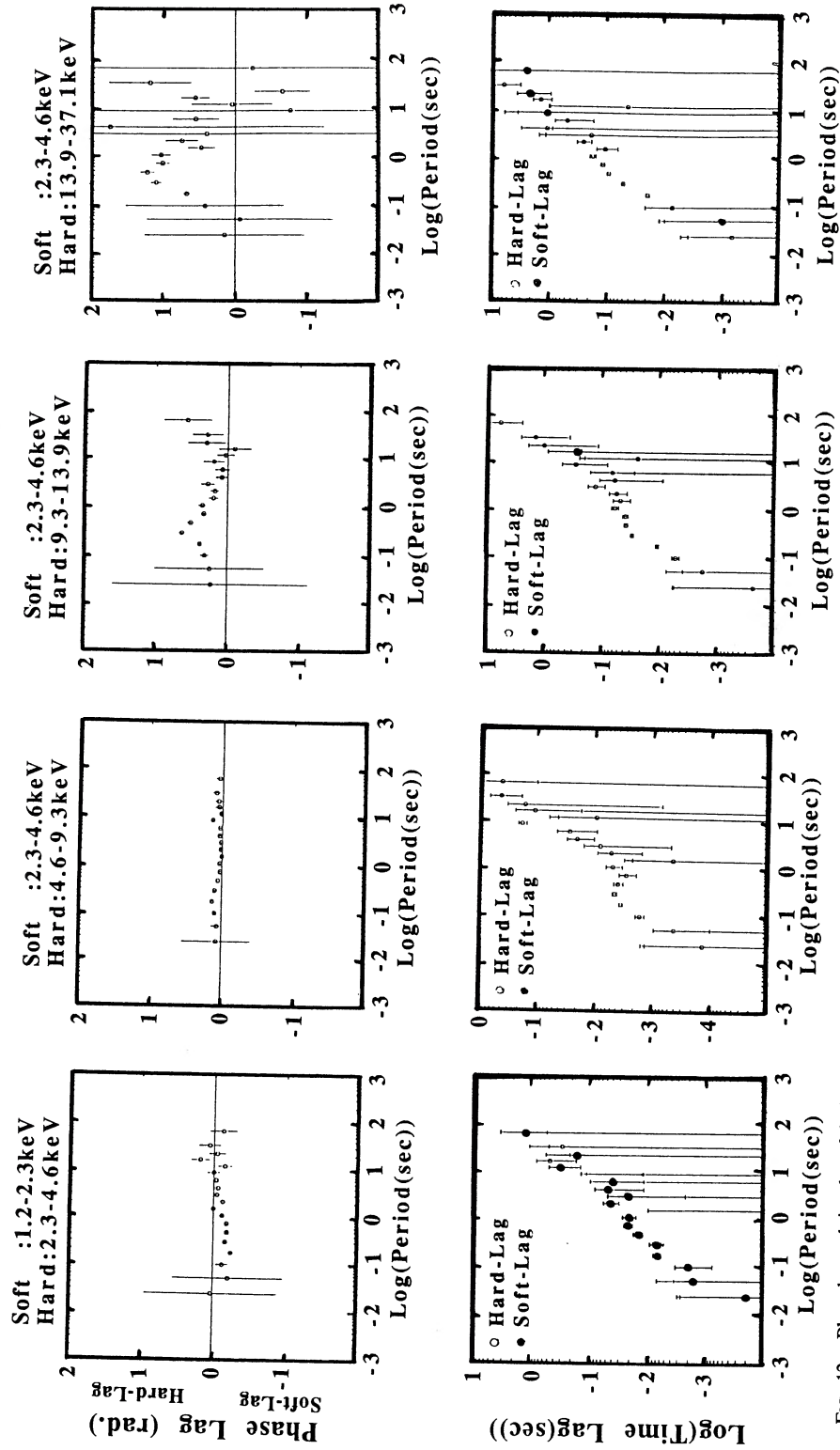
Fig. 12.—Phase lag and time lag of the joint spectral states C and D. (Data: September 5, 12:07–12:12, 13:24–13:53, 14:58–15:22, 15:24–15:29, 16:01–17:04.)

The observed X-ray flux on 1988 September 3–4 is about 2.5×10^{-8} ergs cm^{-2} s^{-1} for 1–30 keV, which corresponds to about 4×10^{-8} ergs cm^{-2} s^{-1} if a correction is made for interstellar absorption. This value corresponds to the Eddington limit of the mass of the X-ray star $M_X/M_\odot = 0.56 \, (D/4 \text{ kpc})^2$, where D is the distance to the X-ray star. The flux can be the Eddington limit for the 5 $M_\odot$ black hole at the distance of 12 kpc, which can be within our Galaxy. Thus the very high state can be the Eddington limit of a black hole if the distance is larger than about 10 kpc.

3.2. *Hardness Ratio Increasing and Decreasing Branches*

Some low-mass X-ray binaries have Z-shaped spectral branches in their color-intensity and color-color diagrams. These are called Z sources, and the branches are called horizontal branch, normal branch, and flaring branch (see, for instance, Lewin, van Paradijs, & van der Klis 1988, Hassinger & van der Klis 1989 and Schulz, Hassinger, & Trümper 1989). GX 339−4 has similar branches in its color-intensity diagram as shown in Figure 5, and the hardness ratio decreasing branch (states D, C, and E) seems to correspond to the horizontal branch and the hardness ratio increasing branch (states G, H, F, and A) seems to correspond to the normal branch of the Z sources. However, in Z sources, QPOs with frequencies of 20–50 Hz are observed in the horizontal branch, and QPOs of about 6 GHz are observed in parts of the normal branch. In the power spectral states A, B, C, and D on the hardness ratio decreasing branch and the crossing point of the two branches in GH 339−4, we also observed QPOs of frequency of about 6 Hz. The color-color relation of the hardness ratio decreasing branch is also different from those of the horizontal branch in low-mass X-ray binaries. Thus the hardness ratio decreasing branch in GX 339−4 is different from the horizontal branch of Z sources.

In the normal branch of GX 5-1 and Cyg X-2, the hardness ratio increases by 30% with the increase of the X-ray flux of 80% in GX 5-1, and the hardness ratio increases by 23% with the increase of the X-ray flux of 8% in Cyg X-2. In the hardness ratio increasing branch (G, H, F, and A) in GX 339−4, the hardness ratio increases from 0.06 to 0.12 (100% increase) during the increase of the X-ray flux from 6400 to 8500 (33% increase). The ratio of these values is similar to that of Cyg X-2. We also observed 6 Hz QPOs in the power spectral state A, which is situated on the crossing region of the hardness ratio increasing and decreasing branches. Thus the hardness ratio increasing branch seems to correspond to the normal branch of Cyg X-2, though we have no information about 6 Hz QPOs in the states G and H in this branch due to the poor time resolution of the observed data.

3.3. *High-Energy Tail as a Compton-scattered Component*

In §§ 2.4 and 2.5, we observed that the time variations of the soft X-ray component and the high-energy X-ray tail are quite different. On time scales of several hours, the intensity of the soft X-ray component changes quite differently from that of the hard tail. On shorter time scales ($\leq$ minutes), the high-energy tail is the cause of the time variation such as dips, flip-flops, and QPOs, and the soft X-ray component shows smaller time variation than the high-energy tail.

Thus we must search for the production mechanism of the high-energy tail, which has apparently no direct relation to the disk blackbody component in the long-term intensity varia-
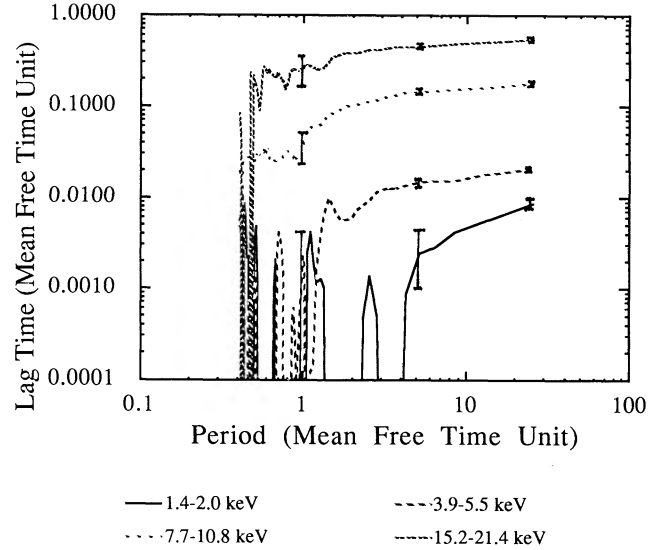

FIG. 13.—Time lags expected from a Compton-scattering model. The time lags from the X-rays of 2.8–3.9 keV are shown. Photons of a blackbody of $kT = 1$ keV are incident to a Compton cloud of $kT_e = 30$ keV and $\tau = 0.5$.

tions, although there is some relation as shown in the color-color and the color-intensity diagrams.

As the spectrum of the hard tail component can be expressed by the model of Compton scattering, we will examine the feasibility of this model to explain the flip-flop and the time lags.

1. *The Flip-Flop Phenomena.*—As for the energy spectra of the high and the low level of the flip-flop state, the values in Table 3 show that during the low level, the number of photons incident to the Compton cloud decreases and the temperature of the Compton cloud increases slightly, which is reasonable if the energy supply to the Compton cloud is constant, i.e., the temperature of the Compton cloud increases due to the decrease in incident photons to the cloud.

2. *The Lag Time.*—To simulate the time lag of variations of the Compton-scattered radiation, we calculated the time lag of the emitted photons from a Compton cloud by a Monte Carlo method in the case that initial photons of a blackbody of $kT = 1$ keV were incident to a uniform and static Compton cloud with electron temperature $kT_e = 30$ keV and a Thomson scattering depth $\tau = 0.5$ and 1.0. The time lag of the photons of various energies relative to those of energies of 2.8–3.9 keV emitted from the Compton cloud were obtained, and the results for $\tau = 0.5$ are shown in Figure 13. The time lag shows a shoulder structure, which is quite similar to the previous calculated results in a different condition of the Compton cloud (Miyamoto et al. 1988), and the time lags of the shoulder are plotted in Figure 14.

We can find in Figure 14 that both the time variations of the X-rays below 2.8 keV and those higher than 3.9 keV show a time lag relative to the time variation of 2.8–3.9 keV X-rays. This is natually expected, because in this model the X-ray photons other than the initial 1 keV blackbody radiation should be delayed since these photons should have suffered at least one Compton scattering in the Compton cloud.

As the shoulder shape of the observed time lag structure shown in Figure 12 is similar to the calculated time lag shown in Figure 13, we assumed that the observed shoulder was due to the Compton scattering and compared the observed time
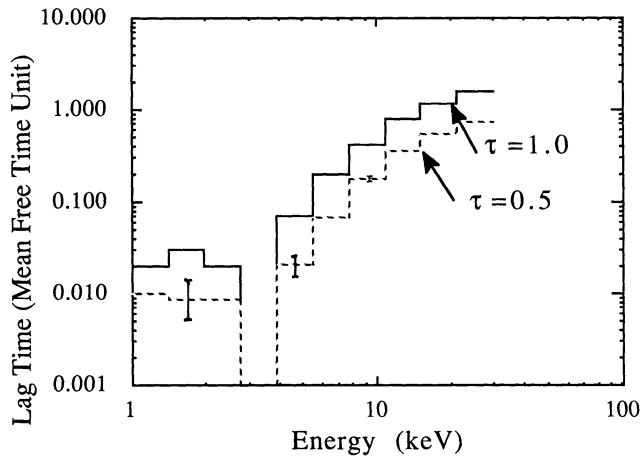
FIG. 14.—Expected time lag from the X-rays of 2.8–3.9 keV. Photons of a blackbody of $kT = 1$ keV are incident to a Compton cloud of $kT_e = 30$ keV.

lag with the results of the Monte Carlo calculation as shown in Figure 15. From the fitting of the data higher than 4.6 keV X-rays, the size of the Compton cloud is estimated to be about 2×10^9 cm with $\tau = 0.5$.

The observed time lag of the time variation of the X-rays below 2.3 keV relative to those of 2.3–4.6 keV X-rays is larger than the simulated value by about a factor of 10. This can be expected if the incident photons have a narrower spectrum than the assumed 1 keV blackbody radiation, and at the X-ray energy of less than 2.3 keV, the fraction of the Comptonized X-rays is larger than that in the simulated calculation.

3.4. *Problems of the Compton-scattering Model*

This Compton-scattering model, however, poses several problems.

The first problem is that if the center of the Compton cloud is near the center of the accretion disk, all of the X-ray–emitting region in the accretion disk should be inside the Compton cloud because of the large radius of the Compton cloud of 2×10^9 cm, and thus all disk blackbody component should be Compton-scattered.
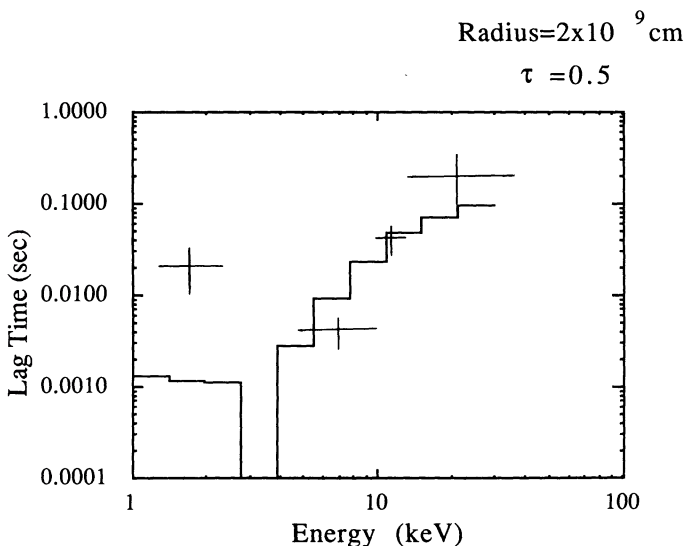

FIG. 15.—A comparison of the observed and the calculated time lags

On the previous model, which was used to fit the X-ray energy spectrum to get Table 2, we assumed that the disk blackbody component did not suffer from Compton scattering. So we examined whether the observed X-ray energy spectrum could be explained by the model in which a disk blackbody component was emitted within the Compton cloud and suffering from the Compton scattering. We chose the model in which the kT of the Compton cloud was 30 keV and the Thomson scattering depth of the cloud was fixed to 0.9 to compute the Compton scattering effect for the disk blackbody component: both the disk blackbody component and the ~ 1 keV black-body radiation are incident to the Compton cloud. The iron line energy and the energy of the K-edge absorption were fixed to 6.5 and 8.8 keV, respectively. We found that this model was acceptable as shown in Table 5.

Thus the Compton-scattering model is possible whether the X-ray–emitting region of the accretion disk is covered by the Compton cloud or not.

The second problem is the source of the energy to the Compton cloud. The energy flux of the high-energy X-ray tail has about 13%–40% of the total X-ray flux as shown in Table 2. And as the fraction of the energy gain per one Compton scattering is about $4kT/mc^2$, the power supplied by the Compton cloud to initial photons, which become the hard tail component after the Compton scatterings, should be $4kT/(mc^2 + 4kT) \times$ (the energy flux of the hard tail). As $4kT/(mc^2 + 4kT) = 0.2$ for $kT = 30$ keV, the power of at least about 3%–7% of the total X-ray energy flux should be supplied to the compton cloud, even if the energy of the initial photons is not supplied by the Compton cloud. As the energy source of the X-ray star is gravitational energy of accreting matter to a compact stars, this power should be supplied from the region within about 10^7 cm of the compact star to the Compton cloud of the size of 2×10^9 cm.

The third problem is that on the time scales of several hours, the time variations of the Comptonized blackbody component are quite different from those of the disk blackbody component as shown in § 2.4. Thus on these time scales the energy supplied to the Compton cloud should not be proportional to the energy supplied to the accretion disk, which is believed to be proportional to the flux of the disk blackbody component.

The fourth problem is that the Comptonized blackbody component shows very rapid variability in spite of the disk blackbody component showing no rapid variation. So we must search for the source of very rapid variations of the incident photons or the Compton cloud. However, this may be solved if the incident photon emitter is the unstable inner edge of the accretion disk (Shibazaki & Hoshi 1975; Shakura & Sunyaev 1976; Pringle 1976).

The second, third, and fourth problems can be explained by a jet model which will be described elsewhere (Miyamoto & Kitamoto 1991). In this jet model, a jet emitting from the central part of the accretion disk is assumed, which is produced by a mechanism such as that as described by Blandford & Payne (1982) or Uchida & Shibata (1985). This jet is the energy source of the Compton cloud, and thus the energy supply to the Compton cloud will not be proportional to the energy supplied to the accretion disk, because other conditions such as local magnetic field strength at the accretion disk may have some effect on development of the jet. This is the cause of the independent time variation of the Comptonized blackbody component and the disk blackbody component. The rapid time variation of the Comptonized blackbody component may

TABLE 5

BEST-FIT PARAMETERS OF THE MODEL

TIME	COMPTONIZED DISK BLACKBODY		COMPTONIZED BLACKBODY			IRON EMISSION LINE	IRON EDGE	ABSORPTION	REDUCED χ^2	INTENSITY (1–37 keV)
	$R_{in}(\cos i)^{1/2}$ (D/4 kpc) km	kT_{in} (keV)	S_{bb} [(D/4 kpc)^2 km^2]	kT_{bb} (keV)	τ	EW (eV)	log N_{Fe} (cm^{-2})	log N_H (cm^{-2})	dof = 37	(counts s^{-1})
Sep 4, 01:56–02:16	47.1 ± 0.4	0.579 ± 0.002	1851 ± 25	0.990 ± 0.003	0.861 ± 0.011	66 ± 21	22.14 ± 0.53	21.77 ± 0.02	2.0808	8485.84
Sep 4, 03:34–03:54	55.3 ± 0.5	0.541 ± 0.002	2276 ± 30	0.959 ± 0.003	0.761 ± 0.009	66 ± 21	22.56 ± 0.24	21.84 ± 0.02	1.8731	8336.20
Sep 4, 05:13–05:33	47.6 ± 0.4	0.583 ± 0.002	1561 ± 24	0.964 ± 0.003	0.892 ± 0.014	64 ± 22	22.43 ± 0.34	21.81 ± 0.02	1.8316	8167.77
Sep 4, 06:49–07:10	47.8 ± 0.4	0.578 ± 0.002	1715 ± 25	0.958 ± 0.003	0.857 ± 0.012	61 ± 20	22.46 ± 0.31	21.79 ± 0.02	2.9843	8152.75
Sep 4, 08:25–08:38	46.5 ± 0.3	0.583 ± 0.002	1640 ± 25	0.984 ± 0.003	0.870 ± 0.014	56 ± 21	20.80 ± 7.50	21.78 ± 0.02	2.1292	8175.53
Sep 4, 08:38–08:49	54.6 ± 1.3	0.548 ± 0.005	1790 ± 87	0.959 ± 0.009	0.805 ± 0.022	71 ± 28	22.71 ± 0.28	21.87 ± 0.03	1.1063	8040.11
Sep 5, 19:58–20:18	50.5 ± 0.4	0.552 ± 0.002	1351 ± 17	1.072 ± 0.003	1.002 ± 0.013	67 ± 21	21.84 ± 1.16	21.75 ± 0.02	1.7886	7758.36
Sep 5, 21:20–21:40	53.1 ± 0.1	0.544 ± 0.001	1482 ± 01	1.049 ± 0.001	0.984 ± 0.001	80 ± 02	21.19 ± 0.87	21.81 ± 0.01	2.2709	7798.56
Sep 5, 21:39–21:43	57.4 ± 1.5	0.533 ± 0.005	1122 ± 61	1.108 ± 0.013	0.982 ± 0.030	61 ± 31	22.66 ± 0.39	21.87 ± 0.03	1.4431	7765.09
Sep 5, 22:46–23:30	69.6 ± 0.7	0.485 ± 0.002	2224 ± 25	0.998 ± 0.002	0.862 ± 0.009	63 ± 22	22.77 ± 0.15	21.90 ± 0.02	1.8667	7747.86
Sep 6, 00:24–00:46	45.1 ± 0.4	0.582 ± 0.002	2178 ± 28	0.967 ± 0.003	0.913 ± 0.012	64 ± 21	22.35 ± 0.48	21.71 ± 0.02	2.0635	8380.42
Sep 6, 02:02–02:12	63.6 ± 4.8	0.506 ± 0.015	2543 ± 28	0.964 ± 0.021	0.844 ± 0.028	63 ± 27	22.87 ± 0.19	21.93 ± 0.04	0.9124	7723.08
Sep 6, 02:12–02:13	47.8 ± 0.5	0.561 ± 0.002	2046 ± 59	0.967 ± 0.006	1.007 ± 0.036	87 ± 35	21.88 ± 1.62	21.72 ± 0.03	0.9087	7705.88
Sep 6, 02:14–02:17	52.6 ± 1.3	0.550 ± 0.005	1026 ± 59	1.140 ± 0.014	1.005 ± 0.030	51 ± 31	22.06 ± 1.52	21.82 ± 0.03	1.1564	7788.30
Sep 6, 02:18–02:24	73.2 ± 2.1	0.481 ± 0.005	1835 ± 80	1.029 ± 0.009	0.854 ± 0.018	55 ± 20	22.82 ± 0.12	21.95 ± 0.02	1.7600	7671.59
Sep 6, 03:40–04:03	45.5 ± 0.4	0.578 ± 0.002	2056 ± 26	0.975 ± 0.003	0.926 ± 0.012	59 ± 21	22.10 ± 0.47	21.72 ± 0.02	2.2909	8228.60
Sep 6, 05:18–05:41	47.0 ± 0.4	0.564 ± 0.002	2277 ± 28	0.958 ± 0.003	0.921 ± 0.011	61 ± 20	22.24 ± 0.51	21.72 ± 0.02	1.7884	7972.03
Sep 6, 06:54–07:18	45.6 ± 0.4	0.580 ± 0.002	1890 ± 23	1.001 ± 0.003	0.875 ± 0.010	56 ± 21	21.85 ± 1.04	21.74 ± 0.02	2.2525	8369.82
Sep 6, 10:08–10:24	63.6 ± 4.9	0.506 ± 0.015	2543 ± 282	0.965 ± 0.021	0.844 ± 0.028	63 ± 27	22.87 ± 0.19	21.93 ± 0.04	0.9125	7723.08
Sep 6, 17:42–17:47	44.5 ± 0.4	0.585 ± 0.002	1960 ± 36	0.973 ± 0.004	0.897 ± 0.018	64 ± 24	22.00 ± 0.92	21.75 ± 0.02	1.3195	8098.67
Sep 6, 18:23–18:44	44.0 ± 0.4	0.588 ± 0.002	1710 ± 25	0.989 ± 0.003	0.891 ± 0.014	56 ± 20	22.13 ± 0.72	21.73 ± 0.02	1.1032	7997.13
Sep 6, 19:38–19:41	48.2 ± 2.9	0.572 ± 0.016	1520 ± 322	0.986 ± 0.037	0.894 ± 0.072	76 ± 36	22.50 ± 0.88	21.83 ± 0.05	0.7690	7754.82
Sep 6, 20:00–20:23	52.9 ± 0.1	0.558 ± 0.001	1190 ± 10	1.001 ± 0.001	0.890 ± 0.001	97 ± 2	21.49 ± 0.29	21.88 ± 0.01	1.5002	7649.16
Sep 6, 21:36–21:59	47.6 ± 0.1	0.582 ± 0.001	1040 ± 10	0.967 ± 0.001	0.964 ± 0.005	89 ± 10	22.23 ± 0.32	21.85 ± 0.01	2.1379	7417.34
Sep 6, 22:53–23:13	49.5 ± 0.3	0.572 ± 0.001	1000 ± 18	0.987 ± 0.004	0.899 ± 0.016	61 ± 22	22.61 ± 0.26	21.87 ± 0.02	2.1980	7381.82
Sep 7, 00:33–00:35	55.2 ± 12.0	0.550 ± 0.005	957 ± 106	0.972 ± 0.020	0.821 ± 0.052	65 ± 37	23.02 ± 0.32	21.87 ± 0.04	0.6667	7192.26
Sep 7, 00:35–00:50	51.0 ± 1.0	0.568 ± 0.004	835 ± 52	0.983 ± 0.013	0.938 ± 0.042	59 ± 26	23.08 ± 0.18	21.90 ± 0.02	0.5977	7178.20
Sep 7, 02:07–02:28	61.0 ± 11.7	0.534 ± 0.003	1812 ± 122	0.775 ± 0.011	0.956 ± 0.048	76 ± 27	23.11 ± 0.12	22.00 ± 0.02	1.2581	6894.68
Sep 7, 03:45–03:46	56.1 ± 7.5	0.543 ± 0.002	1395 ± 121	0.771 ± 0.014	0.924 ± 0.088	75 ± 44	22.39 ± 1.84	21.97 ± 0.02	1.0587	6546.04
Sep 7, 03:50–04:08	61.4 ± 7.1	0.527 ± 0.001	1644 ± 44	0.770 ± 0.005	0.909 ± 0.005	48 ± 23	23.27 ± 0.08	22.01 ± 0.01	1.6158	6590.29
Sep 7, 05:21–05:44	67.7 ± 7.8	0.510 ± 0.001	961 ± 22	0.871 ± 0.004	0.915 ± 0.022	66 ± 22	23.28 ± 0.07	22.05 ± 0.01	2.0916	6520.39
Sep 7, 06:57–07:23	55.3 ± 16.3	0.544 ± 0.009	1184 ± 227	0.811 ± 0.038	1.123 ± 0.120	71 ± 31	23.05 ± 0.34	21.96 ± 0.02	1.3794	6425.85
Sep 7, 08:53–09:02	57.4 ± 10.8	0.540 ± 0.003	1003 ± 78	0.817 ± 0.014	1.168 ± 0.075	69 ± 23	22.95 ± 0.18	22.00 ± 0.02	2.1049	6424.96
Sep 7, 10:15–10:27	57.9 ± 6.7	0.536 ± 0.001	1350 ± 55	0.771 ± 0.007	0.974 ± 0.045	79 ± 26	23.18 ± 0.14	22.00 ± 0.01	1.9225	6321.80

NOTE.—Fixed parameters: Compton cloud for disk blackbody: $kT = 30$ keV, optical depth = 0.9; Compton cloud for blackbody: $kT = 30$ keV; iron line center energy: 6.5 keV; edge energy for iron absorption: 8.8 keV.

be due to time variations of the number of incident photons into the Compton cloud, which are emitted at an unstable inner edge of the accretion disk (Shibazaki & Hoshi 1975; Shakura & Sunyaev 1976; Pringle 1976). This model also explains the rather large absorption due to Fe^{+24} and the iron line as being due to the matter ejected by the jet.

It is possible that the compact star in GX 339−4 is a neutron star and the high-energy tail is emitted at the neutron star surface or the inner edge of the accretion disk very near to the neutron star. In these cases, however, we must explain why the high-energy tail behaves quite differently from the soft disk blackbody component on a time scale of several hours. There must be some mechanism which reserves energy on the neutron star surface or in a nearby part of the accretion disk to the neutron star for several hours and releases the energy gradually. The X-ray bursts are believed to be due to accumulated nuclear fuel on the neutron star surface. However, these phenomena are quite different from the behavior of GX 339−4 in its very high state.

The fifth problem is that there are other components whose time lag is up to about 1 s in the Fourier period of several seconds to several tens of seconds, which cannot be explained by the Compton cloud model, and these are very similar to the time lag observed in Cygnus X-1 (Miyamoto et al. 1988). One possible cause is that the incident photons into the Compton cloud consist of the multi–time constant hardening shots of the time constants of several to tens of seconds, as proposed by Miyamoto & Kitamoto (1989) in the case of Cygnus X-1. Another possible cause is that these components rise from long-term variations of the Compton cloud itself. For instance, if the temperature of the Compton cloud increases gradually and decreases rather suddenly with a time constant of about several seconds to several tens of seconds together with increase and decrease of the incident X-ray photons, the higher energy X-rays will be produced afterward by the Compton scattering, and its causes the hard lag.

The sixth problem is the small time lag of the 6 Hz QPOs compared with those of nearby frequencies in the joint power spectral states C and D. This would be expected in the following situations. We will assume that the QPOs are due to a variation in the number of photons incident to the Compton cloud and the variation is due to oscillations in a part of the source of the photons. Because the delay time of photons emitted from a Compton-scattering cloud is determined by the geometrical size and the Thomson-scattering depth of the Compton cloud, if the geometrical depth or the Thomson-scattering depth of the cloud is smaller at the part of the QPO oscillation in the photon source, a shorter time lag of the QPO component than those in its nearby frequencies is expected. Moreover, if higher energy X-rays are emitting from this oscillating part of the photon source, the harder energy spectrum of the QPO component than the Comptonized blackbody component is also expected.

4. CONCLUSIONS

There is a very high state of GX 339−4, which shows rapid time variations on time scales of less than several minutes, which had not been observed earlier in the high state of this source. We got the following results from the observation of this very high state of this source.

1. The energy spectrum of this state consists of a low-energy component and a high-energy tail, which are consistent with the model in which these are a disk blackbody component and a Comptonized blackbody component, which is produced by a Compton cloud of about 30 keV and a Thomson scattering depth of about 0.5–1.0. The Comptonized blackbody component contains about 13%–40% of the total X-ray energy flux. The energy spectrum also shows K-edge absorption due to Fe^{+24} atoms of about $\log N(Fe^{+24}) = 18.2$–18.9 cm^{-2}. It also has an iron line of equivalent width of 60–100 eV. The fitting results to this model are shown in Table 2. The large K-edge absorption and the iron line in the energy spectrum may be due to the circumstellar gas around the X-ray star.

2. On short time scales less than several minutes, the X-rays show rapid time variations such as dips and flip-flops. The power spectral density functions show 6 Hz QPOs, very low frequency noise (VLF noise), and low-frequency noise (LF noise) as shown in Figure 4. The VLF noise and LF noise are due to the dip- and flip-flop–type time variations. The flip-flop component has a rms amplitude energy spectrum similar to the Comptonized blackbody component, and these intensity changes can be explained to be due to the time variation of the number of incident photons into the Compton cloud. The QPO component has a rms amplitude energy spectrum similar to or harder than that of the Comptonized blackbody component. These energy spectra are shown in Figures 9 and 10.

3. On long time scales larger than hours, the soft disk blackbody component and the hard Comptonized blackbody component change independently as shown in Figure 2 and Table 2. These changes take place in two energy spectral branches: a hardness ratio increasing (with the X-ray flux) branch and a hardness ratio decreasing branch and their crossing region, which are shown in Figure 5. In the hardness ratio increasing branch, the hard Compton-scattering component is the main cause of the change of the X-ray flux on long time scales. On the other hand, in the hardness ratio decreasing branch, the disk blackbody component is the main cause of the change of the X-ray flux. Time variations along these two branches are the cause of the apparent independent time variation of the soft disk blackbody component, and the Comptonized blackbody component on time scales larger than hours.

4. These two energy spectral branches and their crossing region have different types of power spectral density functions: these different branches and their crossing region have different time variations on time scales of less than several minutes. The 6 Hz QPOs exist in the hardness ratio decreasing branch. The existence of QPOs in the hardness ratio increasing branch is not certain because of the poor time resolution of the observed data of this branch, though 6 Hz QPOs exist in the crossing region of the two branches. The flip-flop and the dip together with 6 Hz QPOs are seen at the crossing region of the two branches. The hardness ratio increasing branch seems to correspond to the normal branch of the Z sources of low-mass X-ray binaries.

5. On a lag time versus Fourier period diagram, the time lag between time variations of different energy X-rays shows shoulder structure in addition to the large time lags similar to those observed in Cygnus X-1 as shown in Figure 12. The phase lag and the time lag between the time variations of different X-ray energies show positive lag relative to the X-rays of 2.3–4.6 keV: the time variation of 2.3–4.6 keV energy range is most advanced. These results, except for the large time lag similar to those in Cyg X-1, are consistent with the model in which the high-energy tail is produced by inverse Compton scattering of incident variable blackbody radiation with $kT \sim 1$ keV, the temperature of the hot Compton-scattering

cloud is about 30 keV and its radius is about 2×10^9 cm, though the observed soft lag in the energy range of less than 2.3 keV is much larger than the simulated values. Narrower energy spectrum of the incident photons may be the cause of this large soft lag.

6. The observed energy spectra are consistent with the disk blackbody and Comptonized blackbody model even if the large Compton cloud covers the X-ray–emitting region of the

accretion disk and the disk blackbody component is suffering from Compton scattering.

REFERENCES

Blandford, R. D., & Payne, D. G. 1982, MNRAS, 199, 883
Cowley, A. P., Crampton, D., & Hutchings, J. B. 1987, AJ, 93, 195
Dotani, T. 1989, ISAS Research Note, No. 418
Doxsey, R., et al. 1979, ApJ, 228, L67
Grindlay, J. E. 1979, ApJ, 232, L33
Hassinger, G., & van der Klis, M. 1989, A&A, 225, 79
Hoshi, R. 1984, PASJ, 36, 785
Hutchings, J. B., Cowley, A. P., & Crampton, D. 1981, IAU Circ., No. 3585
Ilovaisky, S. A., & Chevalier, C. 1981, IAU Circ., No. 3586
Ilovaisky, S. A., et al. 1986, A&A, 164, 67
Leahy, D. A., et al. 1983, ApJ, 266, 160
Lewin, W. H. G., van Paradijs, J., & van der Klis, M. 1988, Space Sci. Rev., 46, 273
Maejima, Y., et al. 1984, ApJ, 285, 712
Markert, T. H., et al. 1973, ApJ, 184, L67
Makishima, K., et al. 1986, ApJ, 308, 635
Mitsuda, K. 1989, in Proc. 23rd ESLAB Symp. on Two Topics in X-Ray Astronomy, ed. J. Hunt and B. Battrick (Paris: ESA Publications Division), 197
Mitsuda, K., et al. 1984, PASJ, 36, 741
Mitsuda, K., et al. 1989, PASJ, 41, 97

Miyamoto, S., et al. 1988, Nature, 336, 450
Miyamoto, S., & Kitamoto, S. 1989, Nature, 342, 773
———. 1991, ApJ, 374, 741
Morrison, R., & McCammon, D. 1983, ApJ, 270, 119
Motch, C., Ilovaisky, S. A., & Chevalier, C. 1982, A&A, 109, L1
———. 1985, Space Sci. Rev., 40, 219
Motch, C., et al. 1983, A&A, 119, 171
Nishimura, J., Mitsuda, K., & Itho, M. 1986, PASJ, 38, 819
Nolan, P. L., et al. 1982, ApJ, 262, 727
Pringle, J. E. 1976, MNRAS, 177, 65
———. 1981, ARA&A, 19, 137
Ricketts, M. J. 1983, A&A, 118, L3
Samimi, J., et al. 1979, Nature, 278, 434
Shakura, N. I., & Sunyaev, R. A. 1973, A&A, 24, 337
———. 1976, MNRAS, 175, 613
Shibazaki, N., & Hoshi, R. 1975, Prog. Theor. Phys., 54, 1706
Schulz, N. S., Hassinger, G., & Trümper, J. 1989, A&A, 225, 48
Turner, M. J. L., et al. 1989, PASJ, 41, 345
Uchida, Y., & Shibata, K. 1985, PASJ, 37, 515
van der Klis, M., et al. 1987, ApJ, 319, L13
van Paradijs, J. 1980, A&A, 103, 140